International Journal of Solids and Structures 50 (2013) 3045–3066

Contents lists available at SciVerse ScienceDirect

International Journal of Solids and Structures

journal homepage: www.elsevier.com/locate/ijsolstr

A multi-mechanism model for cutting simulations combining visco-plastic asymmetry and phase transformation

R. Mahnken [a,*], M. Wolff [b], C. Cheng [a]

[a] Chair of Engineering Mechanics, University of Paderborn, Warburger Str. 100, D-33098 Paderborn, Germany
[b] University of Bremen, FB 3 Mathematik/Informatik, Zentrum für Technomathematik, Postfach 330440, D-28334 Bremen, Germany

ARTICLE INFO

Article history:
Received 15 November 2012
Received in revised form 2 May 2013
Available online 23 May 2013

Keywords:
Johnson–Cook
Asymmetric effects
Cutting simulation
Multi phase systems
Phase transformation

ABSTRACT

We develop a multi-mechanism model for strainrate- and temperature-dependent asymmetric plastic material behavior accompanied by phase transformations, which are important phenomena in steel production processes. To this end the well-known Johnson–Cook model is extended by the concept of weighting functions, and it is combined with a model of transformation-induced plasticity (TRIP) based on Leblond's approach. The bulk model is formulated within a thermodynamic framework at large strains, and it will be specialized and applied to cutting processes in steel production. In this prototype situation we have: Transformation of the martensitic initial state into austenite, then retransformation of martensite. For incorporation of visco-plastic asymmetry two variations of the classical Johnson–Cook model are presented: In "Model A" we introduce a rate dependent flow factor with a rate independent yield function. In "Model B" we introduce a rate independent flow factor with a rate dependent yield function. In the examples parameters are identified for the material DIN 100Cr6, and we illustrate the characteristic effects of our multimechanism model, such as strain softening due to temperature, rate dependence and temperature dependence as well as the SD-effect. A finite-element simulation illustrates the different mechanisms for a cutting process.

1. Introduction

In cutting and several other metal working processes the work piece is machined under high speed causing highly inhomogeneous strain rates and temperature, which eventually render residual stresses. Particularly, high speed cutting can change material structural in workpiece surfaces in which white and dark layers are induced due to the intense, localized, rapid thermal–mechanical loading. It has been shown that the white layer and the dark layer consist untempered and overtempered martensite, respectively, due to austenitic transformation and martensitic retransformation Umbrello et al., 2009; Attanasio et al., 2011. To develop three-dimensional constitutive models that account for the finite inelastic deformation of cutting processes, considerable effort was made over the last years. A simple model by Dudzinski and Molinari (1997) considers the shearing produced during the chip formation in orthogonal cutting. Sievert et al. (2003) consider ductile damage at high strain-rates and the influence of the stress-triaxiality on ductile damage. Marusich and Ortiz (1995) introduce a Lagrangian finite element model with remeshing.

A particular role of cutting simulations is played by the well-known Johnson–Cook model Johnson and Cook, 1983, where strain softening is incorporated by a phenomenological modification for the yield stress, see e.g. Behrens et al. (2005), Ozel and Zeren (2004), Hortig (2010), Umbrello et al. (2007) among others. Ramesh et al. (2007) predicted the thickness of white layer taking into account the effects of stress and strain on phase transformation temperatures, where martensitic phase transformation accompanied by the TRIP effect was considered. In addition, more physically-based models are available, such as the Zerilli–Armstrong model Zerilli et al., 1987, which is based on simplified dislocation mechanics. From the above overview we conclude, that the effects of inelastic asymmetry and austenitic phase transformation have not been considered in finite-element cutting simulations. The present article intends to close this gap on the basis of the Johnson–Cook model.

Inelastic asymmetry: Extended experimental tests for high strength steels exhibit different behaviours for different loading types such as tension, compression and shear. For instance, test results for a superalloy Reńe 95 in Stouffer et al. (1996) show, that for merely the same magnitudes of stress in tension and compression the magnitudes of creep rates in tension are much greater than the corresponding rates in compression. A further example is given e.g. in Spitzig et al. (1975) for a martensitic steel, where the yield stress in compression is greater than that in tension. Iwamoto et al. (1998) and Miller and McDowell (1996) obtain the same effect for an austenitc stainess steel. This observation is labelled

* Corresponding author.
E-mail address: rolf.mahnken@ltm.upb.de (R. Mahnken).

0020-7683/$ - see front matter © 2013 Elsevier Ltd. All rights reserved.
http://dx.doi.org/10.1016/j.ijsolstr.2013.05.008

strength-difference effect (SD-effect) or occationally *asymmetric effect*, respectively. It is characterized by the observation, that a certain type of experiment, such as a tension test, is not sufficient in order to characterize the material for different loading scenarios. Instead, additional *independent* types of experiments, such as compression, shear and hydrostatic tests, are necessary in order to get a more comprehensive (though in general still not complete) characterization of the material.

Several publications can be found in the literature for simulation of inelastic material behaviour with asymmetric effects. Most of these approaches are based on a stress potential dependent on the stress tensor and further state variables, which describe e.g. the state of hardening, softening or damage, respectively. Typically, polynomial invariants of the stress tensor are incorporated into the potential. Along this line constitutive equations within the field of plasticity have been formulated e.g. in Spitzig et al., 1975; Altenbach et al., 1995; Mahnken, 2001; Zolochevskii, 1989, amongst others. Approaches for asymmetric effects in creep are suggested in Altenbach et al., 1995; Betten et al., 1998, 1999; Voyiadjis et al., 1998; Voyiadjis et al., 2000; Zolochevsky, 1991, amongst others.

Some publications used the so-called *stress mode angle*, or *Lode angle*, respectively, in order to detect asymmetric effects. This scalar quantity is expressed in terms of the ratio of the second and third basic invariant of the deviatoric stress tensor and is used as an indicator for detection of differences in the loading mode, see e.g. Zolochevskii, 1990; Ehlers, 1995. In Mahnken, 2003 it is used to introduce the concept of *stress mode dependent weighting functions* with the goal to model creep with asymmetric effects. Here an additive decomposition of the inelastic strain rate is assumed, where each of the related quantities incorporates weighting functions dependent on the stress mode angle.

In this work, our objective is to extend the well known Johnson–Cook model Johnson and Cook, 1983 with the concept of weigthing functions introduced in Mahnken, 2003, in order to account for asymmetric effects, e.g. between tension and compression within a large strain framework. To this end, two variations of the classical Johnson–Cook model are presented: In "Model A" we introduce a rate independent flow factor with a rate dependent yield function. The basic idea is the weighting of stress mode dependent material parameters related to viscoplasticity with the above mentioned functions. In "Model B" we introduce a rate dependent flow factor with a rate independent yield function. Here, the basic idea is the weighting of stress mode dependent flow functions related to viscoplasticity with the above mentioned functions. In this way, "Model B" is regarded as an extension of the approoach in Iwamoto et al. (2008), where asymmetric effects in rate dependent behaviour have not been considered.

The advantage of both approaches in "Model A" and "Model B" is, that certain (though not all) material parameters, can be obtained individually from specific loading modes such as tension, compression and shear, investigated experimentally in the laboratory.

Phase transformation: High temperatures also result into phase transformations, which according to the authors knowledge have not been considered for cutting processes. In order to make our approach as general as possible, in this paper we will present a general thermodynamic framework for multi-phase transformation with arbitrary initial phases. Then, in the prototypical situation of our study, the following two phase transformations are taken into account:

1. Transformation of the martensitic initial state into austenite, then
2. retransformation to martensite.

In view of the large heating rate and the relatively high austenitizing temperature, the transformation of the austenite into martensite is described by an approach due to Leblond et al. (1984) and the transformation of martensite is taken into account by the classical relation Koistinen et al. (1959).

The irreversible phase transformations (martensite to austenite and the revers) are characterized by crystallographic rearrangements on the atomistic level, cf. Tjahjanto et al. (2008). On the macroscopical level this effect corresponds to irreversible strains (TRIP strains) of the parent phase, even if the material is loaded by a stress state less than the yield stress of the softer phase. In our approach, we assume that only the softer phase, i.e. austenite, is affected. Several macroscopic constitutive models have been proposed to simulate the complex interactive mechanisms of phase transformation and plasticity, see e.g. Leblond et al. (1984), Tanaka et al. (1985), Fischer et al. (1996); Fischer et al. (1998); Fischer et al. (2000), Hallberg et al. (2007), Wolff et al. (2007), Mahnken et al. (2009), Iwamoto (2004) and to the references therein. Considering micromechanical or multi-scale modeling we refer to Cherkaoui (2002), Turteltaub and Suiker (2005), Tjahjanto et al. (2008).

In a further part of this paper we discuss, how the simultaneous occurence of inelastic strains subjected to compression, tension and torsion modes and inelastic strains due to phase transformation can also be interpreted as a multi-mechanism behavior in the terminology of Cailletaud et al. (1995); Saï et al., 2011. To this end we briefly compare the mathematical structure of our model with the setting in Saï et al., 2011.

This paper is organized as follows:

- Section 2 presents a thermodynamic framework for combined visco-plasticity and multi-phase transformations at large strains. Starting from the multiplicative decomposition of the deformation gradient into inelastic, elastic, thermal and multiphase-transformation parts and assuming a dependence of individual phase densities on pressure, temperature and phase fraction an additive decomposition for the Jacobian of the deformation gradient is derived. This includes concrete expressions for the elastic, thermal and multiphase-transformation parts subject to the constraint of inelastic incompressibility.
- In Section 3, a prototype model is derived by applying the thermodynamic framework to a specific Helmholtz free energy function. For incorporation of visco-plastic asymmetry two variations of the classical Johnson–Cook model are presented: In "Model A" we introduce a rate independent flow factor with a rate dependent yield function. In "Model B" we introduce a rate dependent flow factor with a rate independent yield function. Furthermore, evolution equations for the phase fractions of martensite and austenite will be formulated. Moreover, we discuss the mathematical structure of Model A and Model B as a multi-mechanism model in the sense of Cailletaud et al. (1995) and Saï et al. (2011). Finally, thermodynmic consistency of the proposed model is shown taking multi-phase transformations into account.
- In the examples in Section 4, parameters are identified for the material DIN 100Cr6, and we illustrate the characteristic effects of our multimechanism model, such as strain softening due to temperature, phase transformation, rate dependence and temperature dependence as well as the visco-plastic asymmetry (SD-effect). A finite-element simulation illustrates the different mechanisms for a cutting process.

Notations

Square brackets $[\bullet]$ are used throughout the paper to denote 'function of' in order to distinguish from mathematical groupings with parenthesis $(\bullet)$.

2. A thermodynamic framework for visco-plasticity and phase transformations for multiple phases

2.1. Kinematics

The constitutive equations used in this work are formulated in the framework of a large-strain theory. To this end the deformation gradient $\mathbf{F}$ is introduced at each material point, mapping line segments $d\mathbf{X}$ of the reference configuration $\mathcal{B}_0$ to line segments $d\mathbf{x}$ of the current configuration $\mathcal{B}$, and we introduce its Jacobian $J = \det \mathbf{F}$, mapping a volume element dV of the reference configuration $\mathcal{B}_0$ to a volume element dv of the actual configuration $\mathcal{B}$:

$$1.\ d\mathbf{x} = \mathbf{F} \cdot d\mathbf{X}, \quad 2.\ dv = J dV. \tag{1}$$

The second order deformation gradient can be split multiplicatively as

$$1.\ \mathbf{F} = \mathbf{F}^{\mathrm{vol}} \cdot \mathbf{F}^{\mathrm{iso}} = \mathbf{F}^{\mathrm{iso}} \cdot \mathbf{F}^{\mathrm{vol}},\ \text{where}\ 2.\ \mathbf{F}^{\mathrm{vol}} = J^{1/3}\mathbf{1}. \tag{2}$$

Note, that the tensors $\mathbf{F}^{\mathrm{vol}}$ and $\mathbf{F}^{\mathrm{iso}}$ are interchangeable in Eq. (2.1), which is due to the property $\mathbf{A} \cdot \mathbf{1} = \mathbf{1} \cdot \mathbf{A}, \forall \mathbf{A}$ for the second order unit tensor $\mathbf{1}$ occuring in Eq. (2.2). By construction, $\mathbf{F}^{\mathrm{iso}}$ and $\mathbf{F}^{\mathrm{vol}}$ represent isochoric and volumetric deformations, respectively. For the scenario of phase-transformation coupled to thermo-elasto-visco-plasticity both quantities are split further based on the following assumptions:

1. the elastic deformation is both volumetric and isochoric, represented by J_e and $\mathbf{F}_e^{\mathrm{iso}}$,
2. the thermal deformation is purely volumetric, represented by J_θ,
3. the transformational deformation is purely volumetric, represented by J_z,
4. the plastic deformation is purely isochoric, represented by $\mathbf{F}_i$,
5. there exists a stress free isochoric intermediate configuration.

From the above 5 assumptions we conclude the following decompositions of the isochoric and volumetric part of the deformation gradient:

$$\begin{aligned} &1.\ \mathbf{F}^{\mathrm{iso}} = \mathbf{F}_e^{\mathrm{iso}} \cdot \mathbf{F}_i \\ &2.\ J = J_e \cdot J_\theta \cdot J_z \quad \Rightarrow \quad \mathbf{F}^{\mathrm{vol}} = (J_e \cdot J_\theta \cdot J_z)^{1/3}\mathbf{1}. \end{aligned} \tag{3}$$

Remark 2.1

1. Note, that due to Assumption 2 we do not have to distinguish between total and isochoric contributions for the inelastic part $\mathbf{F}_i$.
2. The tensors $\mathbf{F}_e^{\mathrm{iso}}$ and $\mathbf{F}_i$ in Eq. (3.1) are not interchangeable, which is due to the above Assumption 5.
3. Clearly, the scalar terms in J_e,J_θ and J_i in Eq. (3.1) are interchangeable.
4. Following Levitas et al. (1998) the inelastic part $\mathbf{F}_i$ is closely related to both, visco-plasticity and phase transformation, see also Hallberg et al. (2007).

Inserting Eqs. (3.1) and (3.2) into Eq. (2.1) renders

$$\mathbf{F} = J^{1/3}\mathbf{F}_e^{\mathrm{iso}} \cdot \mathbf{F}_i = (J_e \cdot J_\theta \cdot J_z)^{1/3}\mathbf{F}_e^{\mathrm{iso}} \cdot \mathbf{F}_i. \tag{4}$$

From the first part of this relation we derive

$$\begin{aligned} &1.\ \mathbf{F}_e = J_e^{1/3}\mathbf{F}_e^{\mathrm{iso}}, \quad 2.\ \mathbf{F}_e^{-1} = J_e^{-1/3}(\mathbf{F}_e^{\mathrm{iso}})^{-1}, \\ &3.\ \dot{\mathbf{F}}_e = \frac{1}{3J_e^{2/3}}\mathbf{F}_e^{\mathrm{iso}}\dot{J}_e + J_e^{1/3}\dot{\mathbf{F}}_e^{\mathrm{iso}}, \end{aligned} \tag{5}$$

where the dot above the argument represents the derivative with respect to time t. The time derivatives of the volumetric and isochoric contributions in Eq. (3) are

$$1.\ \dot{\mathbf{F}}^{\mathrm{iso}} = \dot{\mathbf{F}}_e^{\mathrm{iso}} \cdot \mathbf{F}_i + \mathbf{F}_e^{\mathrm{iso}} \cdot \dot{\mathbf{F}}_i. \quad 2.\ \dot{\mathbf{F}}^{\mathrm{vol}} = \frac{1}{3J^{2/3}}\dot{J}\mathbf{1} \tag{6}$$

and consequently from Eq. (4) one obtains

$$\dot{\mathbf{F}} = \left(\frac{1}{3J^{2/3}}\dot{J}\mathbf{F}_e^{\mathrm{iso}} + J^{1/3}\dot{\mathbf{F}}_e^{\mathrm{iso}}\right)\mathbf{F}_i + J^{1/3}\mathbf{F}_e^{\mathrm{iso}} \cdot \dot{\mathbf{F}}_i. \tag{7}$$

With this result and the inverse from Eq. (4)

$$\mathbf{F}^{-1} = J^{-1/3}(\mathbf{F}_i)^{-1} \cdot (\mathbf{F}_e^{\mathrm{iso}})^{-1} \tag{8}$$

the velocity gradient with respect to the actual configuration is

$$\mathbf{l} = \dot{\mathbf{F}} \cdot \mathbf{F}^{-1} = \frac{1}{3}\frac{d}{dt}(\ln J)\mathbf{1} + \dot{\mathbf{F}}_e^{\mathrm{iso}} \cdot \mathbf{F}_e^{\mathrm{iso}^{-1}} + \mathbf{F}_e^{\mathrm{iso}} \cdot \dot{\mathbf{F}}_i \cdot \mathbf{F}_i \cdot (\mathbf{F}_e^{\mathrm{iso}})^{-1}, \tag{9}$$

where the relation $\dot{J}/J = d(\ln J)/dt$ has been used. An elastic pull back renders a velocity gradient with respect to the intermediate configuration

$$\begin{aligned} \bar{\mathbf{L}} &:= \mathbf{F}_e^{-1} \cdot \mathbf{l} \cdot \mathbf{F}_e = (\mathbf{F}_e^{\mathrm{iso}})^{-1} \cdot \mathbf{l} \cdot \mathbf{F}_e^{\mathrm{iso}} \\ &= \frac{1}{3}\frac{d}{dt}(\ln J)\mathbf{1} + \mathbf{F}_e^{\mathrm{iso}^{-1}} \cdot \dot{\mathbf{F}}_e^{\mathrm{iso}} + \dot{\mathbf{F}}_i \cdot \mathbf{F}_i. \end{aligned} \tag{10}$$

By use of

$$\ln J = \ln J_e + \ln J_\theta + \ln J_z \tag{11}$$

and Eq. (5.1) we obtain the following additive decomposition

$$\begin{aligned} &1.\ \bar{\mathbf{L}} := \bar{\mathbf{L}}_e + \bar{\mathbf{L}}_i + \bar{\mathbf{L}}_\theta + \bar{\mathbf{L}}_z, \quad \text{where} \\ &2.\ \bar{\mathbf{L}}_e := \mathbf{F}_e^{-1} \cdot \dot{\mathbf{F}}_e, \quad 3.\ \bar{\mathbf{L}}_i := \dot{\mathbf{F}}_i \cdot \mathbf{F}_i^{-1} = -\mathbf{F}_i \cdot \dot{\mathbf{F}}_i^{-1}, \\ &4.\ \bar{\mathbf{L}}_\theta := \frac{1}{3}\frac{d}{dt}(\ln J_\theta)\mathbf{1}, \quad 5.\ \bar{\mathbf{L}}_z := \frac{1}{3}\frac{d}{dt}(\ln J_z)\mathbf{1}. \end{aligned} \tag{12}$$

Consequently $\bar{\mathbf{L}}_e, \bar{\mathbf{L}}_i, \bar{\mathbf{L}}_\theta, \bar{\mathbf{L}}_z$, represent respectively the elastic, inelastic, thermal and transformation part.

2.2. Volume changes due to pressure, temperature and phase fraction

Let us consider a mixture of $n_z \geqslant 2$ phases (constituents) fulfilling a volume differential dV and having a mass differential dm at the reference configuration. We assume that the mixture is homogeneous, i.e. all phases are equally distributed. The (bulk) densities ρ_0 and ρ of the mixture with respect to the reference and the current configurations are respectively defined as

$$1.\ \rho_0 = \frac{dm}{dV}, \quad 2.\ \rho = \frac{dm}{dv}. \tag{13}$$

Within the volume dv, let the i^{th} phase have its volume dv_i and its mass dm_i. The volume phase fraction $z_i^{(v)}$, the mass phase fraction z_i and the density of the i^{th} phase are defined by

$$1.\ z_i^{(v)} = \frac{dv_i}{dv}, \quad 2.\ z_i = \frac{dm_i}{dm}, \quad 3.\ \varrho_i = \frac{dm_i}{dv_i}. \tag{14}$$

Generally, the mixture is not (spatially) homogeneous. Based on (13) and (14), the quantities $\varrho, z_i^{(v)}, z_i$ and ϱ_i are defined at a body point $\mathbf{X} \in \mathcal{B}_0$ by a limit process with volumes contracting to this point. We assume that such limit process is possible. Thus, these quantities are functions of space, and, clearly, of time. Obviously, the following balances are valid in all body points and for all times,

$$\begin{aligned} &1.\ \sum_{i=1}^{n_z} z_i^{(v)} = 1, \quad 2.\ \sum_{i=1}^{n_z} z_i = 1, \quad 3.\ z_i^{(v)} \geqslant 0, \\ &4.\ z_i \geqslant 0 \quad \text{for all } i = 1, \ldots, n_z. \end{aligned} \tag{15}$$

The mass included in a fixed volume does not depend on possible volume changes due to temperature or strain changes. Thus, the mass phase fractions z_i have the advantage to be independent of temperature and deformation. Moreover, from (13) and (14) a relation between mass and volume phase fractions follows (for all admissible temperatures θ and pressures p)

$$z_i = \frac{\varrho_i[\theta,p]}{\varrho[\theta]} z_i^{(v)}[\theta,p] \quad \text{for all } i=1,\dots,n_z, \tag{16}$$

as well as the following mixture rules for the bulk density ϱ and its inverse are valid

$$1.\ \varrho = \sum_{i=1}^{n_z} \varrho_i z_i^{(v)}, \quad 2.\ \frac{1}{\varrho} = \sum_{i=1}^{n_z} \frac{1}{\varrho_i} z_i. \tag{17}$$

We remark that some of the formulas derived above can also be found in Raniecki et al. (1991). We also remark, that fortunately, due to the small differences of the densities of the steel phases (at the same temperature), the difference between mass and volume fractions ("absolute error") is less than 0.02. The relative error is less than 4.5% in *unfavorable* cases, see Mahnken et al., 2012.

Inserting the relations (13) into Eq. (1.2) and regarding the multiplicative decomposition of the deformation gradient in Eq. (3.2) renders

$$J = \frac{dv}{dV} = \frac{\rho_0}{\rho} = J_e \cdot J_\theta \cdot J_z, \tag{18}$$

where $J_e = \det \mathbf{F}_e, J_\theta = \det \mathbf{F}_\theta, J_z = \det \mathbf{F}_z$, respectively are elastic, thermal and transformation parts.

We assume that the volume dV will be changed by a density change induced by pressure change $p-p_0$, temperature change $\theta-\theta_0$ and/or by and phase fraction change $\underline{z}-\underline{z}_0$, leading to a new volume dv with a new density ρ. Let ρ be a function of pressure p, absolute temperature θ and of mass phase fractions $\underline{z}$ with reference value $\rho_0 = \rho[p_0,\theta_0,\underline{z}_0]$. Upon defining a state vector $\underline{s} = [p,\theta,\underline{z}]$, a Taylor extension up to the first-order terms yields

$$J = \frac{\rho_0}{\rho} \approx 1 - \frac{1}{\rho_0}\frac{\partial \rho}{\partial p}\Big|_{\underline{s}_0}(p-p_0) - \frac{1}{\rho_0}\frac{\partial \rho}{\partial \theta}\Big|_{\underline{s}_0}(\theta-\theta_0) - \frac{1}{\rho_0}\sum_{i=1}^{n_z}\frac{\partial \rho}{\partial z_i}\Big|_{\underline{s}_0}(z_i - z_{0i}). \tag{19}$$

Using the mixture rule for the inverse density in (17) and rearranging, the relation (19) gives

$$\begin{aligned} J = \frac{\rho_0}{\rho} \approx 1 &- \sum_{i=1}^{n_z} \frac{\rho_0 z_{0i}}{\rho_i[p_0,\theta_0]} \left(\frac{1}{\rho_i[p_0,\theta_0]} \frac{\partial \rho_i}{\partial p}[p_0,\theta_0] \right)(p-p_0) \\ &+ \sum_{i=1}^{n_z} \frac{\rho_0 z_{0i}}{\rho_i[p_0,\theta_0]} \left(-\frac{1}{\rho_i[p_0,\theta_0]} \frac{\partial \rho_i}{\partial \theta}[p_0,\theta_0] \right)(\theta-\theta_0) \\ &+ \sum_{i=1}^{n_z} \frac{\rho_0}{\rho_i[p_0,\theta_0]}(z_i - z_{0i}). \end{aligned} \tag{20}$$

Using Eq. (15) the last summand in Eq. (20) can be re-written in accordance with

$$\begin{aligned} \sum_{i=1}^{n_z} \frac{\rho_0}{\rho_i[p_0,\theta_0]}(z_i - z_{0i}) &= \sum_{i=1}^{n_z} \frac{\rho_0}{\rho_i[p_0,\theta_0]} z_i - \sum_{i=1}^{n_z} z_i^{(v)}[p_0,\theta_0] \\ &= \sum_{i=1}^{n_z} \frac{\rho_0}{\rho_i[p_0,\theta_0]} z_i - 1 \\ &= \sum_{i=1}^{n_z} \frac{\rho_0}{\rho_i[p_0,\theta_0]} z_i - \sum_{i=1}^{n_z} z_i \\ &= \sum_{i=1}^{n_z} \left(\frac{\rho_0}{\rho_i[p_0,\theta_0]} - 1 \right) z_i. \end{aligned} \tag{21}$$

Defining the isothermal compressibility of the i^{th} phase $\kappa_i[p_0,\theta_0]$, the bulk compressibility κ, the heat-dilatation coefficient of the i^{th} phase $\alpha_i[p_0,\theta_0]$, the bulk heat-dilatation coefficient α and the mass phase-dilatation coefficient β_{mi} of the i^{th} phase (all related to the reference pressure p_0, to the reference temperature θ_0 and to the reference phase mixture $z_0^{(v)}$) by

$$\begin{aligned} &\kappa[\underline{s}_0] := \sum_{i=1}^{n_z} \frac{\rho_0 z_{0i}}{\rho_i[p_0,\theta_0]} \kappa_i[p_0,\theta_0], \quad \kappa_i[p_0,\theta_0] := \frac{1}{\rho_i[p_0,\theta_0]} \frac{\partial \rho_i}{\partial p}[p_0,\theta_0], \\ &\alpha[\underline{s}_0] := \sum_{i=1}^{n_z} \frac{\rho_0 z_{0i}}{\rho_i[p_0,\theta_0]} \alpha_i[p_0,\theta_0], \quad \alpha_i[p_0,\theta_0] := -\frac{1}{3\rho_i[p_0,\theta_0]} \frac{\partial \rho_i}{\partial \theta}[p_0,\theta_0], \\ &\underline{\beta}[p_0,\theta_0] := [\beta_1,\dots,\beta_{n_z}]^T, \quad \beta_i[p_0,\theta_0] := \frac{1}{3}\left(\frac{\rho_0}{\rho_i[p_0,\theta_0]} - 1 \right), \end{aligned} \tag{22}$$

a compact form of Eq. (20) is

$$J \approx 1 - \kappa[\underline{s}_0](p-p_0) + 3\alpha[\underline{s}_0](\theta-\theta_0) + 3\underline{\beta}^T[p_0,\theta_0]\underline{z} \tag{23}$$

and where the numbers 3 have been introduced for convenience. Next, assuming the approximation $J-1 \approx \ln J$ for small elastic, thermal and transformation strains, the multiplicative form (18) can be transformed by use of (23) into the following additive form

$$\ln J = \ln J_e + \ln J_\theta + \ln J_z \tag{24}$$

$$\approx -\kappa[\underline{s}_0](p-p_0) + 3\alpha[\underline{s}_0](\theta-\theta_0) + 3\underline{\beta}^T[p_0,\theta_0]\underline{z}. \tag{25}$$

In order to take experimental findings into account, we let κ depend on θ in forthcoming considerations.

2.3. Balance relations

In macroscopic modeling of steel behavior, the material is usually regarded as a coexisting mixture of its phases (i.e. constituents). In contrast to general mixtures, the phases do not diffuse. Here, we assume a constant (macroscopic) carbon content.

Using balance relations in a material representation with respect to the reference configuration $\mathcal{B}_0$ we have, see e.g. Haupt (2002)

$$\begin{aligned} &1.\ \varrho_0 \ddot{\mathbf{u}} - \mathrm{Div}(\mathbf{F}\cdot\mathbf{S}) = \varrho_0 \mathbf{f}, \quad \text{(linear momentum)} \\ &2.\ \varrho_0 \dot{e} + \mathrm{Div}\mathbf{q}_0 = \mathbf{S} : \dot{\mathbf{E}} + \varrho_0 r_\theta, \quad \text{(energy)} \\ &3.\ -\varrho_0 \dot{e} + \varrho_0 \theta \dot{\eta} + \mathbf{S} : \dot{\mathbf{E}} - \frac{1}{\theta}\mathbf{q}_0 \cdot \mathrm{Grad}\theta \geqslant 0. \quad \text{(entropy)} \end{aligned} \tag{26}$$

In addition to the above notations we use: ϱ_0 – density in the reference configuration, $\mathbf{u}$ – displacement vector, $\mathbf{E} = (1/2)(\mathbf{F}\cdot\mathbf{F}-\mathbf{1})$ – Green strain tensor, $\mathbf{S}$ – (symmetric) 2nd Piola–Kirchhoff stress tensor, $\mathbf{f}$ – mass density of external forces, e – mass density of the internal energy, $\mathbf{q}_0$ – heat-flux density vector, r_θ – mass density of heat supply. The dot above the argument denotes its time derivative. We also recall, that the inequality 26.3 is known as the *Clausius–Duhem inequality*.

We assume the following functional relation for the Helmholtz free energy Ψ be given by

$$\Psi = \Psi[\overline{\mathbf{C}}_e, \underline{q}, \underline{z}, \theta], \tag{27}$$

where $\overline{\mathbf{C}}_e = \mathbf{F}_e^T \cdot \mathbf{F}_e$ is the elastic right Cauchy–Green tensor, $\underline{q} = [q_i,\dots,q_{n_q}]$ is a vector of hardening internal variables of strain type. The vector $\underline{z} = [z_1, z_2, \dots, z_{n_z},]$ introduced in Section 2.2 considers the different n_z phases, and also plays the role of an internal variable. Next, we note the constitutive relations for the Mandel stress tensor $\overline{\mathbf{M}}$ and the entropy η and define thermodynamic forces $\underline{Q} = [Q_1, Q_2, \dots, Q_{n_q}]^T$ and $\underline{Z} = [Z_1, Z_2, \dots, Z_{n_z}]^T$:

$$1.\ \overline{\mathbf{M}} = \rho_0 2\overline{\mathbf{C}}_e \cdot \frac{\partial \Psi}{\partial \overline{\mathbf{C}}_e},\quad 2.\ \eta = -\frac{\partial \Psi}{\partial \theta},\quad 3.\ \underline{Q} = \rho_0 \frac{\partial \Psi}{\partial \underline{q}},$$
$$4.\ \underline{Z} = \rho_0 \frac{\partial \Psi}{\partial \underline{z}}. \tag{28}$$

The thermodynamic forces Q_i are called hardening stresses and the quantities Z_i are named chemical forces. The relations (28.1) and (28.2) result from the Clausius–Duhem inequality by standard arguments, see e.g. Mahnken et al. (2012). The following inequalities are sufficient for the validity of the Clausius–Duhem inequality (26.3)

$$1.\ \mathcal{D}^i = \overline{\mathbf{M}} : \bar{\mathbf{L}}_i - \underline{Q}\dot{\underline{q}} - \underline{Z}\dot{\underline{z}} \geqslant 0,\quad 2.\ \mathcal{D}^\theta = -\frac{1}{\theta}\mathbf{q}_0 \cdot \mathrm{Grad}\theta \geqslant 0. \tag{29}$$

A common approach for the heat flux vector in Eq. (29.2) is the Fourier-law with respect to the reference configuration $\mathbf{q}_0 = -\lambda_\theta (\det \mathbf{F})\mathbf{C}^{-1} \cdot \mathrm{Grad}\theta$, where λ_θ a non-negative heat conduction coefficient. In a general setting it is necessary to formulate evolution equations

$$1.\ \bar{\mathbf{L}}_i = \bar{\mathbf{L}}_i[\overline{\mathbf{M}}, Q, \underline{Z}, \underline{q}, \underline{z}, \theta],\quad 2.\ \dot{\underline{q}} = \dot{\underline{q}}[\overline{\mathbf{M}}, \underline{Q}, \underline{Z}, \underline{q}, \underline{z}, \theta],$$
$$3.\ \dot{\underline{z}} = \dot{\underline{z}}[\overline{\mathbf{M}}, \underline{Q}, \underline{Z}, \underline{q}, \underline{z}, \theta], \tag{30}$$

which are in accordance with the Clausius–Planck inequality 29.1, such that the model under consideration becomes thermodynamically consistent. In the framework above the evolution equations are formulated in terms of the Mandel stress tensor $\overline{\mathbf{M}}$, the hardening stresses $\underline{Q}$ and the chemical forces $\underline{Z}$, which appear as conjugate (dual) variables to $\bar{\mathbf{L}}_i, \dot{\underline{q}}$ and $\dot{\underline{z}}$ in Eq. (29.1).

Following Cailletaud et al. (1995) and Saï et al. (2011) the terminology "multi-mechanism" is used when different behaviors are observed in the material. These behaviors may be linked to different strain ranges, different stress ranges, different temperatures, etc. Concerning the mathematical structure of a multi-mechanism model in Saï et al. (2011), an *nMmC* model is obtained with n mechanisms (i.e. number of inelastic strain contributions) and m criteria (i.e. number of yield functions): Accordingly, the above velocity gradient is additively decomposed as

$$\bar{\mathbf{L}}_i = \sum_{j=1}^{n} \bar{\mathbf{L}}_{in\,j}. \tag{31}$$

We will return to this issue in Section 3.9.

2.4. Heat-conduction equation

The heat-conduction equation can be derived in a standard way from the energy Eq. (26.2) (cf. e.g. Haupt (2002)). Taking the Eq. (28) into account and expressing the stress power as $\mathcal{P} = \mathbf{S} : \dot{\mathbf{E}} = \overline{\mathbf{M}} : \bar{\mathbf{L}}$, one gets from Eq. (26.2):

$$\rho_0 c_d \dot{\theta} + \mathrm{Div}\mathbf{q}_0 = \overline{\mathbf{M}} : \bar{\mathbf{L}}_i - \underline{Q}\dot{\underline{q}} - \underline{Z}\dot{\underline{z}} + \theta \frac{\partial \overline{\mathbf{M}}}{\partial \theta} : \bar{\mathbf{L}}_e + \theta \frac{\partial \underline{Q}}{\partial \theta}\dot{\underline{q}} + \theta \frac{\partial \underline{Z}}{\partial \theta}\dot{\underline{z}} + \rho_0 r_\theta$$

with the heat capacity

$$c_d := -\theta \frac{\partial^2 \Psi}{\partial \theta^2} \left(= \frac{\partial e}{\partial \theta} \right). \tag{33}$$

Eq. (32) will be further specialized in Section 3.9.

3. A prototype model for cutting processes

The general thermodynamic framework of the previous section is now specialized to the scenario of a cutting process. To this end, we make concrete proposals for the Helmholtz free energy as well as for the evolution of internal variables. Finally, we discuss the thermodynamic consistency of the model developed below.

In the cutting process under consideration, there are mainly two phases, numbered as follows:

$$\begin{array}{ll} A & \text{for austenite} \\ M & \text{for martensite.} \end{array} \tag{34}$$

Consequently, the total number of phases introduced in the previous subsection becomes $n_z = 2$.

3.1. Helmholtz free energy

The Helmholtz free energy Ψ describes the energy storage due to small reversible deformations of the crystal lattice as well as inelastic deformations. More generally, it can also be used to describe different storage mechanisms, e.g. energy changes due to interfacial effects or dislocations. As a specific example of a Helmholtz free energy function we consider, see e.g. Raniecki et al. (1991) and Fischer et al. (1996):

$$1.\ \Psi = \Psi^{iso}[\overline{\mathbf{C}}_e, \underline{z}, \theta] + \Psi^{vol}[\overline{\mathbf{C}}_e, \underline{z}, \theta] + \Psi^{\theta}[\theta] + \Psi^{p}[\underline{q}, \underline{z}, \theta] + \Psi^{ch}[\underline{z}, \theta],\ \text{where}$$
$$2.\ \Psi^{iso} = \frac{G[\theta]}{4\rho_0}\left(\mathrm{tr}\left[\ln \hat{\mathbf{C}}_e\right]^2\right)$$
$$3.\ \Psi^{vol} = \frac{1}{2\rho_0}K[\theta](\ln J_e)^2$$
$$4.\ \Psi^{\theta} = \int_{\theta_0}^{\theta} c_d[\bar{\theta}]d\bar{\theta} - \theta\int_{\theta_0}^{\theta}\frac{c_d[\bar{\theta}]}{\bar{\theta}}d\bar{\theta}$$
$$5.\ \Psi^{p} = \Psi^{p1} + \Psi^{p2} = \frac{1}{2\rho_0}H_1 q_1^2 + \frac{1}{2\rho_0}H_2 q_2^2.$$
$$6.\ \Psi^{ch} = \sum_{i=1}^{2}(z_i - z_{0i})\phi_{ch,i}[\theta]. \tag{35}$$

Remark 3.1

1. The elastic part $\Psi^{el} = \Psi^{iso} + \Psi^{vol}$ takes storage quantities related to the elastic strains into account. The part Ψ^{iso} in Eq. (35.2) considers isochoric deformations due to isochoric elastic strains, where $\hat{\mathbf{C}}_e = J_e^{-2/3}\overline{\mathbf{C}}_e$. The part Ψ^{vol} in Eq. (35.3) considers volumetric strains represented by J_e defined in Eq. (1.2). Furthermore, $G[\theta]$ and $K[\theta] = \kappa[\theta]^{-1}$ are the shear modulus and the compression (or bulk) modulus, respectively, both dependent on temperature θ. These are related to Young's modulus E, Poisson's ratio ν and the compressiblity κ as

$$1.\ G[\theta] = \frac{2E[\theta]}{1+\nu},\quad 2.\ K[\theta] = \frac{E[\theta]}{3(1-2\nu)} = \kappa[\theta]^{-1}. \tag{36}$$

We employ a linear dependence of Young's modulus as

$$E = E_0 + c_E(\theta - \theta_0), \tag{37}$$

where θ_0 is the reference temperature of Section 2 and c_e is a constant. We remark, that the above ad hoc extension for the bulk modulus 36.2 could also be included in the definition (22)

2. Assuming the approximation $\ln J \approx J - 1$, i.e. we assume that the volumetric changes due to elasticity, temperature and/or phase transformation are small, the additive decomposition (25) yields

$$\Psi^{vol} = \frac{1}{2\rho_0}K[\theta](\ln J_e)^2 = \frac{1}{2\rho_0}K[\theta](\ln J - \ln[J_\theta J_z])^2$$
$$\approx \frac{1}{2\rho_0}K[\theta]\left(\ln J - 3\left(\alpha[\underline{s}_0](\theta - \theta_0) + \underline{\beta}^T[p_0, \theta_0]\underline{z}\right)\right)^2. \tag{38}$$

3. We assume the same elastic isotropic behavior for all phases in Eq. (35.2) (similarly as in Hallberg et al. (2007)). Consequently, it suffices to take into account the temperature dependence as introduced in Eq. (37), a dependence of G and K on the phase-fraction vector $\underline{z}$ is not used.
4. The term Ψ^{θ} in Eq. 35.4 represents thermally stored energy. Here, we neglect the phase dependence of the specific heat capacity c_d. To be consistent with the approach in 35.6, the term Ψ^{θ} refers to the initial state, e.g. to martensite (cf. point 6 of these remarks).
5. The inelastic part Ψ^{p} of the Helmholtz free energy is defined in Eq. (35.5). It accounts for energy storage due to inelastic deformations, more concretely to combined linear and nonlinear isotropic hardening. q_1 and q_2 are (scalar) internal variables of strain type, such that its number is $n_q = 2$. The evolution will be described below. Note, that there is a technical difference to the presentation in Mahnken et al. (2009), but the sum of the thermodynamical forces Q_1 and Q_2 (cf. Eq. (28.1)) finally equals to the single force Q in Mahnken et al., 2009. Q_0, b and H are positive constants.
6. The term Ψ^{ch} in Eq. 35.6 represents the chemically stored energy with respect to phase transformations. In case of no phase transformations, i.e. for $\underline{z} = \underline{z}_0$, this term does not appear.

3.2. Thermodynamic forces

As discussed previously in Section 2 the thermodynamic forces are obtained from the relations (28). Consequently, from Eq. (28.1) and Eq. (38) the Mandel stress tensor is

$$\begin{aligned}\overline{\mathbf{M}} &= \rho_0 2\overline{\mathbf{C}}_e \cdot \frac{\partial \Psi}{\partial \overline{\mathbf{C}}_e} \\ &= K[\theta]\ln J\mathbf{1} + G[\theta]\mathrm{dev}\ \ln\left[\overline{\mathbf{C}}_e\right] \\ &\quad - 3K[\theta]\left(\alpha[\underline{s}_0](\theta-\theta_0) + \underline{\beta}^T[p_0,\theta_0]\underline{z}\right)\mathbf{1}. \end{aligned} \tag{39}$$

The first two terms in Eq. (39) represent the spherical and deviatoric stress tensors due to deformations.

The third term accounts for thermo-mechanical and chemo-mechanical coupling, respectively.

From the Eq. (28.3) and (28.4), (38), and (35.5) and (35.6) we identify the hardening stresses and the chemical forces as

$$\begin{aligned} &1.\ Q_1 = \rho_0 \frac{\partial \Psi^p}{\partial q_1} = H_1 q_1, \quad 2.\ Q_2 = \rho_0 \frac{\partial \Psi^p}{\partial q_2} = H_2 q_2, \\ &3.\ Z_i = \rho_0 \frac{\partial \Psi}{\partial z_i} = -K[\theta]\left(\frac{\rho_0}{\rho_i[\theta_0]} - 1\right)\ln J_e + \rho_0 \phi_{ch,i}[\theta], \quad i = M, A. \end{aligned} \tag{40}$$

Remark 3.2.

1. Applying the "trace-"operator $\mathrm{tr}[\bullet] = \mathbf{1} : [\bullet]$ to Eq. (39), renders the pressure as

$$\begin{aligned} -3p &= \mathrm{tr}\overline{\mathbf{M}} \\ &= 3K[\theta]\left(\ln J - 3\left(\alpha[\underline{s}_0](\theta-\theta_0) + \underline{\beta}^T[p_0,\theta_0]\underline{z}\right)\right) \end{aligned} \tag{41}$$

which for $p_0 = 0, \theta = \theta_0$ is in accordance with Eq. (25).

2. As we will see later, the two terms on the right-hand side of Eq. (40.1) represent nonlinear and linear isotropic hardening, respectively.
3. For steel (see Mahnken et al., 2012; Mahnken et al., 2012) and small elastic strains we have

$$\begin{aligned} &\left(\frac{\rho_0}{\rho_i[\theta_0]} - 1\right) \approx 0, \quad J_e \approx 1 \Rightarrow K[\theta]\left(\frac{\rho_0}{\rho_i[\theta_0]} - 1\right)\ln J_e \\ &\qquad \approx 0 \Rightarrow Z_i \approx \rho_0 \phi_{ch,i}[\theta]. \end{aligned} \tag{42}$$

4. The chemical force $Z_i \approx \rho_0 \phi_{ch,i}$ can be regarded as (volume density of) the free enthalpy of the phase z_i. (This fact relies on the Gibbs–Duhem relation, we refer to Nolting, 2010; de Groot et al., 1984; Raniecki et al., 1991, amongst others).

In the process under consideration with two phase, the balance relation 15.1, relates the rate of austenite to the rate of martensite as

$$\dot{z}_A = -\dot{z}_M. \tag{43}$$

This allows writing the following relation:

$$-\sum_{i=1}^{2} Z_i \dot{z}_i = -Z_M \dot{z}_M - Z_A \dot{z}_A = -(Z_M - Z_A)\dot{z}_M. \tag{44}$$

Thus, employing the approximation (42) for the chemical forces Z_i, the dissipation term related to phase transformations in Eq. (29) can be re-written as

$$-\sum_{i=1}^{2} Z_i \dot{z}_i = -(Z_M - Z_A)\dot{z}_M \approx -\rho_0(\phi_{ch,M} - \phi_{ch,A})\dot{z}_M. \tag{45}$$

A possible relation for the chemical force difference $Z_M - Z_A$ is

$$Z_M - Z_A = \rho_0(\phi_{ch,M} - \phi_{ch,A}) = \rho_0(\theta - \theta_0^{(M,A)})\frac{Q_{M,A}^*}{\theta_0^{(M,A)}}. \tag{46}$$

Here $\theta_0^{(M,A)}$ is defined as the equilibrium temperature, at which the martensitic phase has the same free enthalpy as the austenite. Consequently, the temperature difference $(\theta - \theta_0^{(M,A)})$ is the "undercooling" or the "overheating", respectively. Furthermore, in Eq. (46) $Q_{M,A}^*$ is the activation energy for the transformation $M \to A$. It is assumed to be positive, which is a plausible assumption, since a phase transformation only takes place, if the free enthalpy of the parent phase is greater than the free enthalpy of the generated phase. We will return to this point when discussing thermodynamic consistency of the model in Section 3.7 as well as when dealing with the special case of the heat-conduction equation in Section 3.9.

3.3. A yield function of Johnson–Cook type

In Johnson and Cook, 1983 the following (original) relation is proposed for the von Mises stress σ_v:

$$\begin{aligned} &1.\ \sigma_v = (A + B e_v^n)(1 - (\theta^*)^m)\left(1 + C\ln\left(\frac{\dot{e}_v}{\dot{\varepsilon}_0}\right)\right), \\ &2.\ \theta^* = \begin{cases} 0 & \text{for } \theta < \theta^r \\ \frac{\theta - \theta^r}{\theta^m - \theta^r} & \text{for } \theta^r \leqslant \theta \leqslant \theta^m \\ 1 & \text{for } \theta > \theta^m. \end{cases} \end{aligned} \tag{47}$$

Here θ^* is the homologous temperature, θ^r is the room temperature and θ^m is the melt temperature of the material, respectively, and $A, B, n, C, \varepsilon_0, m$ are six material parameters. A is the initial yield stress (subsequently denoted as Y_0), and B and n represent the effect of strain hardening. C and ε_0 represent the effect of rate dependency for the yield stress, whereas m represents the effect of adiabatic heating. The above formulation accounts for rate and temperature dependency.

From the original Johnson–Cook function (47), we formulate a yield function

$$1.\ \phi = \sigma_v - (Y_0 + Q_1 + Q_2)\mathcal{J}\quad 2.\ \mathcal{J} = \mathcal{J}^\theta \mathcal{J}^R$$
$$3.\ \mathcal{J}^\theta = (1-(\theta^*)^m)\quad 4.\ \mathcal{J}^R = \left(1 + C\ln\left(\left\langle\frac{\dot e_v}{\dot\varepsilon_0}\right\rangle_1\right)\right),$$

where the von Mises stress is written in terms of the deviatoric part of the Mandel stress tensor as

$$\sigma_v = \sqrt{\frac{3}{2}}\|\overline{\mathbf{M}}^{dev}\|. \tag{49}$$

Subsequently, the coefficient $\mathcal{J}$ in Eq. (48.2) shall be refered to as the Johnson–Cook coefficient, where $\mathcal{J}^\theta$ and $\mathcal{J}^R$ reflect the dependences of temperature and strain rate, respectively.

Remark 3.3

1. Comparing Eq. (47) and Eq. (48) we introduce as a first modification, that the hardening stress Be_v^n in Eq. (47) is replaced by the sum of hardening stresses Q_1 and Q_2 introduced in the relations (40).
2. Comparing Eq. (47) and Eq. (48) we introduce as a further (slight) modification the notation $x_1 = \max\{x, 1\}$. This ensures the relation

$$\mathcal{J} = (1-(\theta^*)^m)\left(1 + C\ln\left(\left\langle\frac{\dot e_v}{\dot\varepsilon_0}\right\rangle_1\right)\right) \geqslant 0 \tag{50}$$

for all parameters $C \geqslant 0, \varepsilon_0 > 0, m > 0$, and all temperatures $\theta > 0$.

3.4. Evolution equations for visco-plasticity

We split the inelastic part $\bar{\mathbf{L}}_i$ of the velocity gradient $\bar{\mathbf{L}}$ into the sum

$$\bar{\mathbf{L}}_i = \bar{\mathbf{L}}_p + \bar{\mathbf{L}}_t, \tag{51}$$

where $\bar{\mathbf{L}}_p$ and $\bar{\mathbf{L}}_t$ represent the visco-plastic and the TRIP part, respectively. In the following we propose evolution equations for both quantities. Within this approach, we extend the well-known Johnson–Cook model in order to take into account asymmetric effects for plasticity, based on the concept of stress-mode related weighting functions introduced in Mahnken, 2003.

3.4.1. Stress mode related weighting functions

Following the approach of Mahnken (2003) for the weighting functions w_i it is stipulated that

$$1.\ \sum_{i=1}^{S} w_i[\overline{\mathbf{M}}] = 1,\quad 2.\ w_i[\overline{\mathbf{M}}_j] = \delta_{ij},\quad 3.\ w_i[\overline{\mathbf{M}}] \geqslant 0, \tag{52}$$

i.e. the weighting functions w_i are associated to different independent characteristic *stress modes* characterised by stress tensors $\overline{\mathbf{M}}_j, j = 1, 2, .., S$. We also remark, that Eq. (52.1) can be regarded as a *completeness condition*, whereas Eq. (52.2) constitutes a *normalisation condition* for the weighting functions. The specific mathematical structures for weighting functions have been introduced in Mahnken, 2003 on the basis of the following quantities:

$$1.\ \xi = \frac{\sqrt{27}}{2}\frac{{}^{\overline{M}_{dev}}I_3}{\left({}^{\overline{M}_{dev}}I_2\right)^{3/2}}$$
$$2.\ {}^{\overline{M}_{dev}}I_i = \frac{1}{i}\mathbf{1} : \left(\overline{\mathbf{M}}^{dev}\right)^i,\quad i = 2, 3. \tag{53}$$

The quantity ξ is refered to as the *stress mode factor* and has the property $-1 \leqslant \xi \leqslant 1$. Related graphical interpretations are given in Mahnken, 2003.

For the stress modes related to the loading scenarios of tension, compression and shear we set $S = 3$. Then the requirements (52) are satisfied by the following weighting functions in terms of the stress mode factor ξ:

$$1.\ \text{tension}:\ w_1[\xi] = \begin{cases}\xi^2, & \text{if } \xi \geqslant 0\\ 0, & \text{else}\end{cases}$$
$$2.\ \text{compression}:\ w_2[\xi] = \begin{cases}\xi^2, & \text{if } \xi \leqslant 0\\ 0, & \text{else}\end{cases} \tag{54}$$
$$3.\ \text{shear}:\ w_3[\xi] = 1 - \xi^2$$

For the case, that experimental data are available only for the loadings in tension and compression, with $S = 2$ the following functions are used

$$1.\quad \text{tension}:\ w_1[\xi] = \tfrac{1}{2}(1+\xi)$$
$$2.\quad \text{compression}:\ w_2[\xi] = \tfrac{1}{2}(1-\xi). \tag{55}$$

3.4.2. Evolution of internal variables

We assume the following evolution equations for the visco-plastic part $\bar{\mathbf{L}}_p$ of the velocity gradient in Eq. (51) and the internal variables q_1 and q_2 in the relation (35.4)

$$1.\ \bar{\mathbf{L}}_p = \dot\lambda\sqrt{\frac{3}{2}}\overline{\mathbf{N}},\quad \text{where } \overline{\mathbf{N}} = \frac{\overline{\mathbf{M}}^{dev}}{\|\overline{\mathbf{M}}^{dev}\|},$$
$$2.\ \dot q_1 = \dot\lambda\mathcal{J}\left(1 - c\frac{Q_1}{H_1}\right), \tag{56}$$
$$3.\ \dot q_2 = \dot\lambda\mathcal{J},$$

where $\mathcal{J}$ is the Johnson–Cook coefficient in Eq. (50.2). Furthermore, the plastic multiplier $\dot\lambda$ is obtained from the loading/unloading conditions, see e.g. Simo et al., 1998,

$$1.\ \dot\lambda \geqslant 0,\quad 2.\phi \leqslant 0,\quad 3.\ \dot\lambda\phi = 0. \tag{57}$$

Here, we have also introduced the rate of equivalent plastic strain $\dot e_v$, defined as $\dot e_v^2 = 2/3\ \bar{\mathbf{L}}_p : \bar{\mathbf{L}}_p$, such that by use of Eq. (56.1) one obtains the relation

$$\dot e_v = \sqrt{\frac{2}{3}\bar{\mathbf{L}}_i : \bar{\mathbf{L}}_i} = \dot\lambda\sqrt{\frac{2}{3}\frac{3}{2}\overline{\mathbf{N}} : \overline{\mathbf{N}}} = \dot\lambda. \tag{58}$$

Remarks 3.4

1. The coefficient $c \geqslant 0$ in Eq. (56.2) may depend on the temperature and different quantities, e.g. invariants of the stress tensor.
2. Here, we consider positive constant parameters H_1 and H_2. A dependence on temperature is possible, while a dependence on further quantities would result in more terms in the Clausius–Planck inequality (29.1).
3. As explained in Mahnken (2005) an alternative mixed-variant representation of the above flow rule 56.1 relative to the reference configuration $\mathcal{B}_0$ is as follows:

$$1.\ \mathbf{L}_{in} = \mathbf{F}_i^{-1}\cdot\bar{\mathbf{L}}_i\cdot\mathbf{F}_i = -\frac{1}{2}\dot{\mathbf{C}}_i^{-1}\cdot\mathbf{C}_i = \dot\lambda\mathbf{N},\quad \text{where}$$
$$2.\ \mathbf{N} = \frac{\mathbf{M}^{dev}}{\|\mathbf{M}^{dev}\|} \tag{59}$$
$$3.\ \mathbf{C}_i = \mathbf{F}_i^t\cdot\mathbf{F}_i,$$

This representation is more convenient with respect to numerical implementation in order to get an objective time-integration scheme Simo et al., 1998.

According to the relations (40.1), (40.2), (56.2) and (56.3) one obtains

$$\begin{aligned} &1.\ \dot{Q}_1 = H_1\dot{q}_1 = \dot{\lambda}\mathcal{J}(H_1 - cQ_1) \\ &2.\ \dot{Q}_2 = H_2\dot{q}_2 = \dot{\lambda}H_2\mathcal{J} \end{aligned} \tag{60}$$

For the special case $\mathcal{J} = 1, H_1, H_2$ and $c > 0$ being constant, and the initial conditions $Q_1(0) = 0, Q_2(0) = 0$ one obtains the solutions

$$\begin{aligned} &1.\quad Q_1(e_v) = \tfrac{H_1}{c}(1 - \exp(-ce_v)) \\ &2.\quad Q_2(e_v) = H_2 e_v. \end{aligned} \tag{61}$$

With the stress mode related weighting functions in the Eqs. (53), (55) and evolution of the hardening stresses in (60) at hand we are in a position to formulate two extended variations of the original Johnson–Cook model based on Eq. (47).

3.4.3. Model A: rate independent flow factor with a rate dependent yield function

Table 1 summarizes all equations for the first proposel for simulation of asymmetric visco-plasticity, labeled Model A in the sequel: It consists of a flow rule in Eq. (I), with flow direction in Eq. (II) and flow factor in Eq. (III). The yield function in Eq. (IV) constitutes a barrier term for the von Mises stress σ_v in Eq. (V), written in terms of the Mandel stress tensor $\overline{\mathbf{M}}$. The scalar Y_0 in Eq. (IV) represents an initial barrier for inelastic behavior, which is increased by the hardening stresses Q_1 and Q_2 in Eq. (VI). The total barrier $Y_0 + Q_1 + Q_2$ may be decreased or increased by the Johnson–Cook coefficient $\mathcal{J}$ in Eq. (VII). Rate dependence of Model A is achieved by the factor $\mathcal{J}^R$. The key idea of Model A is obtained by the weighted constants in Eq. (VIII). All related material parameters are summarized in Eq. (IX).

3.4.4. Model B: rate dependent flow factor with a rate independent yield function

Table 2 summarizes all equations for the second type of asymmetric visco-plasticity. Compared to Model A, the key idea here is an additive decomposition of the flow factor in Eq. (IV) into a sum of S stress mode related quantities. The flow factors for each mode in Eq. (III) are formulated as standard power laws and render the rate dependence for the model. Furthermore the notation $< x > = x$ for $x > 0, < x > = 0$ for $x \leqslant 0$ has been used, such that the function $\Phi = \Phi[\overline{\mathbf{M}}, Q]$ in Eq. (V) plays the role of an *overstress function*. Note, that for simplicity the flow direction in Eq. (II) and the flow factor in Eq. (III) are assumed to be identical for all stress modes. Contrary to Model A, the hardening stresses Q_1 and Q_2 in Eq. (VII) consider only the temperature part $\mathcal{J}^\theta$ of the Johnson–Cook coefficient in Eq. (VIII), since rate dependence is activated by the power laws in Eq. (III). All material parameters of Model B are summarized in Eq. (IX).

Table 1
Model A: Rate independent flow factor with a rate dependent yield function

(I)	Flow rule	$\overline{\mathbf{L}}_p = \dot{\lambda}\sqrt{\frac{3}{2}}\overline{\mathbf{N}}$
(II)	Flow direction	$\overline{\mathbf{N}} = \frac{\overline{\mathbf{M}}^{dev}}{\|\overline{\mathbf{M}}^{dev}\|}$
(III)	Flow factor	$\dot{\lambda} = \dot{e}_v = \sqrt{\frac{2}{3}\overline{\mathbf{L}}_p : \overline{\mathbf{L}}_p}$
(IV)	Yield function	$\Phi = \sigma_v - (Y_0 + Q_1 + Q_2)\mathcal{J}$
(V)	von Mises stress	$\sigma_v = \sqrt{\frac{3}{2}}\|\overline{\mathbf{M}}^{dev}\|$
(VI)	Hardening stresses	$\dot{Q}_1 = \dot{\lambda}\mathcal{J}(H_1 - cQ_1), \dot{Q}_2 = \dot{\lambda}H_2\mathcal{J}$
(VII)	Johnson–Cook coefficient	$\mathcal{J} = \mathcal{J}^\theta\mathcal{J}^R, \mathcal{J}^\theta = \left(1 - (\theta^*)^m\right)$
		$\mathcal{J}^R = \left(1 + C\ln\left(\frac{\dot{e}_v}{\dot{e}_{0_1}}\right)\right)$
(VIII)	Weighted constants	$Y_0 = \sum_{i=1}^{S} w_i Y_{0i}$, $c = \sum_{i=1}^{S} w_i c_i$, $C = \sum_{i=1}^{S} w_i C_i$, $\dot{e}_0 = \sum_{i=1}^{S} w_i \dot{e}_{0i}$, $m = \sum_{i=1}^{S} w_i m_i$
(IX)	Material parameters	$\kappa_{pi} = [Y_{0i}, H_1, H_2, c_i, C_i, \dot{e}_{0i}, m_i]^T$, $i = 1, \ldots, S$

Table 2
Model B: Rate dependent flow factor with a rate independent yield function

(I)	Flow rule	$\overline{\mathbf{L}}_p = \dot{\lambda}\sqrt{\frac{3}{2}}\overline{\mathbf{N}}$
(II)	Flow direction	$\overline{\mathbf{N}} = \frac{\overline{\mathbf{M}}^{dev}}{\|\overline{\mathbf{M}}^{dev}\|}$
(III)	Flow factor for each mode	$\dot{\lambda}_i = \left(\frac{<\Phi>}{K_i}\right)^{n_i}$
(IV)	Weighted flow factor	$\dot{\lambda} = \sum_{i=1}^{S} w_i\dot{\lambda}_i = \dot{e}_v$
(V)	Overstress function	$\Phi = \sigma_v - (Y_0 + Q_1 + Q_2)\mathcal{J}^\theta$
(VI)	von Mises stress	$\sigma_v = \sqrt{\frac{3}{2}}\|\overline{\mathbf{M}}^{dev}\|$
(VII)	Hardening stress	$\dot{Q}_1 = \dot{\lambda}\mathcal{J}^\theta(H_1 - cQ_1), \dot{Q}_2 = \dot{\lambda}H_2\mathcal{J}^\theta$
(VIII)	Johnson–Cook coefficient	$\mathcal{J}^\theta = \left(1 - (\theta^*)^m\right)$
(IX)	Material parameters	$\kappa_{pi} = [Y_0, H_1, H_2, c, c_\theta, K_i, n_i, m]^T$, $i = 1, \ldots, S$

3.5. A flow rule for transformation plasticity

A general flow rule for the transformation part $\overline{\mathbf{L}}_t$ occurring in Eq. (51) can be written as

$$\overline{\mathbf{L}}_t = \sum_{i=1}^{n_z}\overline{\mathbf{L}}_{t,i}, \tag{62}$$

where $\overline{\mathbf{L}}_{t,i}$ represents transformations strains due to transformation of the ith phase, see e.g. Mahnken et al., 2012 for multiple transformations strains. In this paper, we assume that TRIP is only caused by martensitic transformations, neglecting possible TRIP during the formation of austenite. In case of necessity, TRIP caused by austenitic transformation can be included without difficulties. Thus, we suppose

$$\overline{\mathbf{L}}_t = \dot{z}_M\frac{3}{2}f_1' K_{tpM}[\sigma_v]\ (\overline{\mathbf{M}}^{dev})^t. \tag{63}$$

In this way, the term $\overline{\mathbf{L}}_t$ in Eq. (63) generalizes the TRIP approach due to Leblond (1989) among others within a small strain theory. The scalar K_{tpM} in Eq. (63) is the Greenwood–Johnson parameter (Greenwood and Johnson (1965)). A dependence on the stress σ_v has been introduced in Mahnken et al. (2009) in order to obtain a better agreement with experimental results as follows:

$$K_{tpM}[\sigma_v] = K_{tp1M} + K_{tp2M}\sigma_v. \tag{64}$$

The saturation function $f_1[z_M]$in Eq. (63) is a heuristic function satisfying

$$1.\ f_1[0] = 0, \quad 2.\ f_1[1] = 1, \quad 3.\ f_1'[z_M] = \frac{df_1}{dz_M} \geqslant 0. \tag{65}$$

A possible formulation is given by Denis et al. (1983) as

$$1.\ f_1[z_M] = (2 - z)z \Rightarrow 2.\ f_1'[z_M] = 2(1 - z), \quad 3.\ f_1''[z_M] = -2. \tag{66}$$

For further discussions and references concerning TRIP we refer to Wolff et al. (2009).

3.6. Evolution of phase fractions

The cutting forming process under consideration is characterized by two phase transformations generally being dependent of each other: Transformatiom of the martensitic initial state into austenite and retransformation to martensite. There are a lot of different phenomenological (macroscopic) approaches for phase transformations in steel. For discussion and references we refer

Wolff et al. (2007). In the following we give some specific formulations for both phases according to the numbering (34).

In our setting, austenite can only be formed from the martensitic initial state due to conversion of mechanical dissipation into heat during the cutting process. Thus, we set the initial conditions

$$\underline{z}_0 = [z_{M0}, z_{A0}] = [1, 0]^T. \tag{67}$$

As a consequence of Eq. (67), the initial density ρ_0 equals to $\rho_M[\theta_0]$. Moreover, in the elastic part $\Psi^{el} = \Psi^{iso} + \Psi^{vol}$ of the free energy (see (Eq. 35.3)) as well as in Eq. (39) and Eq. (40) some specifications occur. For instance, Ψ^{el} now reads as

$$\Psi^{el} = \frac{G[\theta]}{4\rho_M[\theta_0]}\left(\mathrm{tr}\left[\ln \hat{\mathbf{C}}_e\right]^2\right) + \frac{K[\theta]}{2\rho_M[\theta_0]}(\ln J - (3\alpha_M[\theta](\theta-\theta_0) + K_{tv} z_A))^2. \tag{68}$$

Here the constant

$$K_{tv} = \left(\frac{\rho_M[\theta_0]}{\rho_A[\theta_0]} - 1\right) \tag{69}$$

represents the volume change ratio $\Delta V/V$ after complete transformation for a two phase system, see e.g. Mahnken et al., 2010.

1. Formation of austenite: The heating is very fast and leads to high temperatures. Therefore, for the evolution of the austenite phase fraction z_A we suppose a simple approach due to Leblond et al. (1984)

$$\dot{z}_A = \mu_{MA}(1 - z_A)H(\theta - A_{c1}), \tag{70}$$

where $\mu_{MA} > 0$ is a constant, A_{c1} is the austenite start temperature. The Heaviside function H with $H(s) = 1$ for $s > 0$ and $H(s) = 0$, otherwise, plays the role of a switcher.

2. Formation of martensite: Martensite can only be formed from austenite during rapid cooling due to the contact between work-piece and tool, namely near the surface. We use a rate form of the Koistinen-Marburger approach

$$\dot{z}_M = \left\langle \frac{-\dot{\theta}}{k_\theta} \right\rangle (1 - z_M)H(\theta_{MS} - \theta). \tag{71}$$

Here, $k_\theta > 0$ is the Koistinen–Marburger parameter, and θ_{MS} is the martensite start temperature. In Eq. (71) we assume, that the total amount of martensite transforms into austenite and thus is available for retransformation into martensite. Otherwise, the term $(1 - z_M)$ could be replaced by $(z_A - z_M)$.

3.7. Thermodynamic consistency

For thermodynamic consistency of model A and B under consideration it is sufficient, that the Clausius-Plank inequality (29.1) is fulfilled. In the sequel, we basically follow the approach in Mahnken et al., 2012. Using the split (51), the evolution Eq. (63) for TRIP, (56.2), (56.3) for the internal variables q_1 and q_2, the Clausius–Planck inequality (29.1) for model A re-writes as

$$\mathcal{D}^i = \overline{\mathbf{M}} : \bar{\mathbf{L}}_i - Q_1\dot{q}_1 - Q_2\dot{q}_2 - \sum_{i=1}^{2} Z_i\dot{z}_i = \underbrace{\dot{\lambda}(\sigma_v - (Q_1+Q_2)\mathcal{J})}_{\geqslant Y_0\mathcal{J}} + \dot{\lambda}c\frac{Q_1^2}{H_1}\mathcal{J} + \left(\dot{z}_M\frac{3}{2}f_1' K_{tpM}[\sigma_v]\right)\|\overline{\mathbf{M}}^{dev}\|^2 - \sum_{i=1}^{2} Z_i\dot{z}_i \geqslant 0. \tag{72}$$

Analogously, for model B the Clausius–Planck inequality (29.1) renders

$$\mathcal{D}^i = \overline{\mathbf{M}} : \bar{\mathbf{L}}_i - Q_1\dot{q}_1 - Q_2\dot{q}_2 - \sum_{i=1}^{2} Z_i\dot{z}_i = \underbrace{\dot{\lambda}(\sigma_v - (Q_1+Q_2)\mathcal{J}^\theta)}_{\geqslant Y_0\mathcal{J}^\theta} + \dot{\lambda}c\frac{Q_1^2}{H_1}\mathcal{J}^\theta + \left(\dot{z}_M\frac{3}{2}f_1' K_{tpM}[\sigma_v]\right)\|\overline{\mathbf{M}}^{dev}\|^2 - \sum_{i=1}^{2} Z_i\dot{z}_i \geqslant 0. \tag{73}$$

Due to $K_{tpM} > 0$ the first three terms in (72) and (73) are non-negative. Therefore, it remains to investigate the identical last term of both equations. Using the approximation (42), the assumption (46) and re-writing this term in accordance with (45), it remains to proof that

$$-\sum_{i=1}^{2} Z_i\dot{z}_i = -\rho_0\sum_{i=1}^{2}\left(\theta - \theta_0^{(i,2)}\right)\frac{Q i, 2^*}{\theta_0^{(i,2)}}\dot{z}_i \geqslant 0. \tag{74}$$

Since the activation energies $Q_{i,2}^*$ are assumed to be positive, each summand in (74) is non-negative (taking the minus sign in front of the sum into account). Indeed, for the transformation $M \to A$ (initial state to austenite), the temperature θ is higher than the equilibrium temperature $\theta_0^{(i,2)}$ and z_M decreases, i.e. $\dot{z}_M \leqslant 0$. Contrary, during the transformations $A \to M$ (austenite to martensite), ones has $\theta_0^{(M,A)} > \theta$ and $\dot{z}_M \geqslant 0$. It is well-known that the formation of martensite is not an equilibrium reaction, and there must be a considerable undercooling. Thus, the martensite-start temperature θ_{MS} is much less than $\theta_0^{(M,A)}$. However, this does not contradict our reasoning at the macroscopic level.

Thus, model A and B under consideration are thermodynamically consistent. Moreover, this result does not depend on special approaches for the evolution equations for the phase fractions like Leblond–Devaux, Johnson–Mehl–Avrami–Kolmogoroff or Koistinen–Marburger.

3.8. Interpretation as a multi-mechanism model

As mentioned in Section 2.3 the terminology "multi-mechanism" is used when different behaviors are observed in the material, linked to different strain ranges, different stress ranges, different temperatures, etc. Accordingly, this list of macroscopic effects can extended to compression, tension and torsion modes and moreover to phase transformation, as proposed in our prototype model.

Consequently, the evolution equation for the inelastic part of the velocity gradient $\bar{\mathbf{L}}_i$ of our prototype model B can also be recast as the additive decomposition in Eq. (31). To this end we combine the equations for the inelastic part $\bar{\mathbf{L}}_p$ in Eq. (51) with the flow rule in Table 2 for model B and the transformation part in Eq. (62). This renders the additive decomposition

$$\bar{\mathbf{L}}_i = \sum_{j=1}^{S} w_j\left(\frac{<\Phi>}{K_j}\right)^{n_j}\overline{\mathbf{N}} + \sum_{j=1}^{n_z}\bar{\mathbf{L}}_{t,j}. \tag{75}$$

Thus, we have $n = S + n_z$ mechanisms corresponding to S stress modes and n_z phase-transformations. According to the overview in Table 2, the number of yield criteria is $m = 1$.

For Model A in Table 1, the stress-modes are not explicitly related to the additive decomposition in Eq. (75), however, an implicit relation is obtained by the stress mode dependent material parameters in Table 1.

To the authors knowledge, up to now the theory of multi-mechanism models has been developed only in the framework of small deformations (see Saï et al. (2011)). In this setting, the possible coupling of the mechanisms via the coupling of individual back stresses is characteristic and allows to describe observable interactions. For an application to steel behaviour we refer to Wolff et al. (2011). A corresponding application to finite deformations with coupled kinematic hardening remains to future work.

3.9. Special form of the heat-conduction equation

In our case of two phases involved in the process, we can re-write the heat-conduction Eq. (32), expressing again the austenite rate. This gives

$$\rho_0 c_d \dot{\theta} + \mathrm{Div}\mathbf{q}_0 = \overline{\mathbf{M}} : \bar{\mathbf{L}}_i - \underline{Q}\underline{q} + \theta \frac{\partial \overline{\mathbf{M}}}{\partial \theta} : \bar{\mathbf{L}}_e + \theta \frac{\partial \underline{Q}}{\partial \theta}\underline{\dot{q}} + \sum_{i=1}^{2} L_{i2}\dot{z}_i + \rho_0 r_\theta, \tag{76}$$

where the *latent heat* L_{i2} of the transformation $A \rightarrow M$ is introduced as

$$L_{MA} := \left(-Z_M + Z_A + \theta \frac{\partial Z_M}{\partial \theta} - \theta \frac{\partial Z_A}{\partial \theta} \right). \tag{77}$$

Clearly, the relation $L_{AA} = 0$ holds. Using the approximation (42) and the assumption (46) one gets (in case of constant $Q^*_{i,2}$) from (77):

$$L_{MA} = \rho_0 Q^*_{M,A}. \tag{78}$$

Thus, (the volume density of) the activation energy $\rho_0 Q^*_{M,A}$ of the transformation $A \rightarrow M$ is the latent heat of the corresponding transformation. This assertion corresponds to the observation, that the formation of martensite is exotherm. Contrary, the formation of austenite is endotherm.

In our case, the isotropic hardening stresses do not depend on temperature. Thus, we can finally write the heat-conduction equation in the following form.

$$\rho_0 c_d \dot{\theta} + \mathrm{Div}\,\mathbf{q}_0 = \overline{\mathbf{M}} : \bar{\mathbf{L}}_i - \mathbf{Q}\,\dot{q} + \theta \frac{\partial \overline{\mathbf{M}}}{\partial \theta} : \bar{\mathbf{L}}_e + \sum_{i=1}^{2} L_{i2}\dot{z}_i + \rho_0 r_\theta. \tag{79}$$

3.10. Summary of constitutive equations

The constitutive relations of our multimechanism model are formulated relative to the intermediate configuration $\bar{\mathcal{B}}$ are summarized in Eq. (I) to Eq. (VI) of Table 3.

In Table 3 also the material parameters are summarized. For simplicity, we use a constant for the thermal expansion $\alpha_M[\theta]$. It should also be noted that there are some limitations on the applicability of the equations in Table 3 for general loading paths, especially unloading. However, for the sake of simplicity and assuming that for the cutting process more or less proportional loading paths are to be expected, they will serve as a working assumption in this paper.

Table 3
Multimechanism model for visco-plasticity and transformation-induced plasticity at large strains.

I. Mandel stress tensor
1. $\overline{\mathbf{M}} = K[\theta]\ln J_e \bar{\mathbf{1}}' + G[\theta]\mathrm{dev}\ln\left(\overline{\mathbf{C}}_e\right)$
   - $K[\theta](3\Delta\theta\alpha_M[\theta] + K_{tv}z_A)\mathbf{1}$
2. $G(\theta) = \frac{2E(\theta)}{1+\nu}$, $K(\theta) = \frac{E(\theta)}{3(1-2\nu)}$, $E = E_0 + c_E(\theta - \theta_{E_0})$

II. Inelastic flow
Additive decomposition
1. $\bar{\mathbf{L}}_i = \overline{\mathbf{L}}_p + \overline{\mathbf{L}}_t$
Visco-plastic flow: see Model A in Table 1 or Model B in Table 2
TRIP flow
11. $\overline{\mathbf{L}}_t = \dot{z}_M \frac{3}{2} f_1' K_{tpM}[\sigma_v](\overline{\mathbf{M}}^{dev})^t$
12. $K_{tpM}[\sigma_v] = K_{tp1M} + K_{tp2M}\sigma_v$
13. $f_1'[z] = 2(1 - z_M)$

III. Phase transformation (PT) kinetics
Martensite $\rightarrow$ Austenite ($M \rightarrow A$):
1. $\dot{z}_A = \mu_{MA}(1 - z_A)H(\theta - A_{c1})$
Austenite $\rightarrow$ Martensite ($A \rightarrow M$):
2. $\dot{z}_M = \frac{-\dot{\theta}}{k_\theta}(1 - z_M)H(\theta_{MS} - \theta)$

IV. Material parameters
1. $\kappa_{el} = [E_0, c_E, \theta_{E_0}, \nu]^T$
2. $\kappa_\theta = [\alpha_M]^T$
3. $\kappa_{tp} = [K_{tp1M}, K_{tp2M}, \mu_{MA}, k_\theta]^T$
4. $\kappa_{tc} = [\lambda_\theta, c_d]^T$
5. $\kappa_{co} = [\theta^m, \theta^r, \rho_M, \rho_A, A_{c1}, \theta_{MS}]^T$

The constitutive equations in Table 3 have been implemented into a Finite-Element program using an implicit Euler scheme for time integration. The resulting algorithm is very similar to the approaches in Mahnken, 2005; Mahnken, 2005; Mahnken et al., 2010 and therefore shall not be described in this paper.

4. Representative examples

In this section two numerical examples are presented. In the ensuing Section 4.1 experimental data for a steel 100Cr6 are used for parameter identification of the constitutive equations of the previous Section 3. In a second example the material model is applied in Section 4.2 in order to investigate a cutting process.

4.1. Steel 100Cr6 under tension, compression and shear as well as phase-transformation

This section exhibits simulations of the material behavior for steel 100Cr6 with our multi-mechanism modell. The chemical composition of the material 100Cr6 is listed in Table 4:.

As a main goal the corresponding material parameters are identified. To this end two sets of experimental data have been used:

1. *Thermal–mechanical tests*: This set of experiments takes into account different temperatures, strain rates and stress modes (e.g. tension, compression and torsion). However, only data for temperatures below A_{c3} are available, and thus only valid for pure martensite.
2. *Dilatometer tests*: The second set of experiments covers a broad temperature range – above and below the martensitic start temperature M_s – thus taking into account the TRIP effect. However, stresses are below the yield stress of the two phase material. Furthermore, we note, that the behaviour of phase transformation subjected to the conditions of high rates, as in the cutting process has not been considered so far experimetally.

4.1.1. Thermal–mechanical tests

For the first set, data are available for compression, tension and shear in order to account for the SD-effect. Furthermore, tests were performed at different strain rates and different temperatures in order to account for rate and temperature effects. Concerning specimen geometry and performence of the experiments we refer to Halle (2005). So far experimental results are available with data according to the following nomenclature:

Notation	Strain rate (s^{-1})	Compression (c)/ tension (t) /Shear (s)	Temperature (°C)
t-R0001-T20	0.001	Tension	20
t-R120-T20	120	Tension	20
c-R0001-T20	0.001	Compression	20
c-R01-T20	0.1	Compression	20
c-R184-T20	184	Compression	20
c-R1890-T20	1890	Compression	20
c-R183-T400	183	Compression	400
c-R185-T600	185	Compression	600
s-R101-T20	101	Shear	20
s-R101-T600	101	Shear	600

All specimens and samples used in the experiments are made and provided by the project partner IWF from the Technical University of Berlin in the frame of the german research network

Table 4
Chemical composition of 100Cr6

C %	Si %	Mn %	P %	S %	Cr %	Mo %	Ni %	Al %	Cu %	Ti %
0.97	0.19	0.41	0.01	0.01	1.43	0.05	0.10	0.01	0.11	<0.001

SPP1480. All tests were performed by the company NORDMETALL, Adorf, Germany. In the sequel we give a brief overview on performence of the experiments.

Tension tests: The quasi-static tensile tests at strain rates of 0.001 s^{-1} and at room temperature are performed using a mechanical universal testing machine with a maximum load of 100 kN. The dynamic-impact tensile tests are performed using a rotating wheel machine. Fig. 1(a) shows the schematic illustration of the testing device. It consists of a flywheel, in which a claw is locked at the beginning of the test. The flywheel is accelerated with an electrical drive to the required speed. If the testing velocity is reached, the claw is released and is aligned due to the acting centrifugal force. As the lower part of the specimen is fixed in a pile, the specimen is deformed abruptly, when the claw impacts the pile. Due to the high energy capacity of the flywheel machine, the material is deformed until failure without a significant loss of the impact velocity.

Compression tests: For the investigations under compressive loading, specimens with a diameter of ϕ6 mm and a height of ca. 6.5 mm are used. The quasi-static and quasi-dynamic tests at strain rates of 0.001 and 0.1 s^{-1} are performed on a universal testing machine with a maximum load of 100 kN. The forces were measured using a calibrated load cell. The impact dynamic compression tests at strain rates of ca. 10^2 s^{-1} are performed using a drop weight machine. A schematic illustration of the testing device is shown in Fig. 1(b). A falling mass (B) of 600 kg is guided in a four column frame (A). The punch (C) is mounted on the lower side of the falling mass and impacts the specimen (E), which is adjusted to an anvil (D). After the deformation of the specimen, the mass is stopped by mechanical stopping devices (F) and caught by a hydraulic brake. Using this technique, a second impact of the mass to the specimen is avoided and the deformed specimen can be used for further investigations, e.g. microstructure analysis. The dynamic force is measured directly on the punch (C). The dynamic deformation is measured using an electro-optical gage (G). Beside room temperature testing, the drop weight machine was also used for dynamic compression tests at elevated temperatures. The specimens were heated up using an inductive coil setup.

High dynamic compression tests at strain rates $> 10^3$ s^{-1} were performed using a Split-Hopkinson-Pressure-Bar setup (SHPB), which is schematically shown in Fig. 2(a). A striker bar impacts an incident bar and an elastic pressure wave is developed. The pressure wave propagates through the incident bar and reaches the specimen, which is located between the incident and the transmitter bar. As the amplitude of the incoming pressure wave is larger than the yield strength of the specimen, the specimen is deformed plastically. Hence, a part of the incoming stress wave is transmitted to the transmitter bar and the other part is reflected as a tensile stress wave in the incident bar. Applying the principles

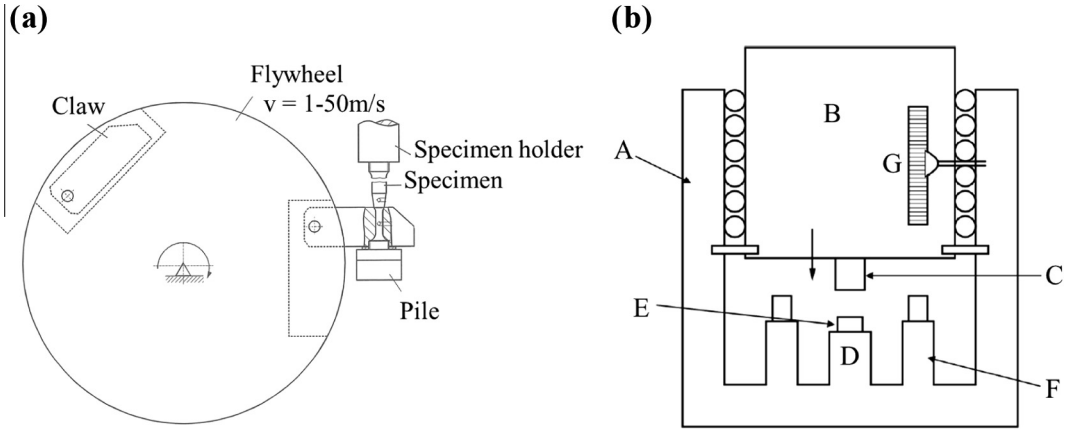

Fig. 1. Test devices: a) Principle of high-rate tensile testing with flywheel setup Handbook, 2002, b) Scheme of a drop weight machine used for dynamic compression loading at ca. 200 s^{-1}: (A) frame, (B) drop weight, (C) punch, (D) anvil, (E) specimen, (F) stopping device, and (G) incremental gage Handbook, 2002.

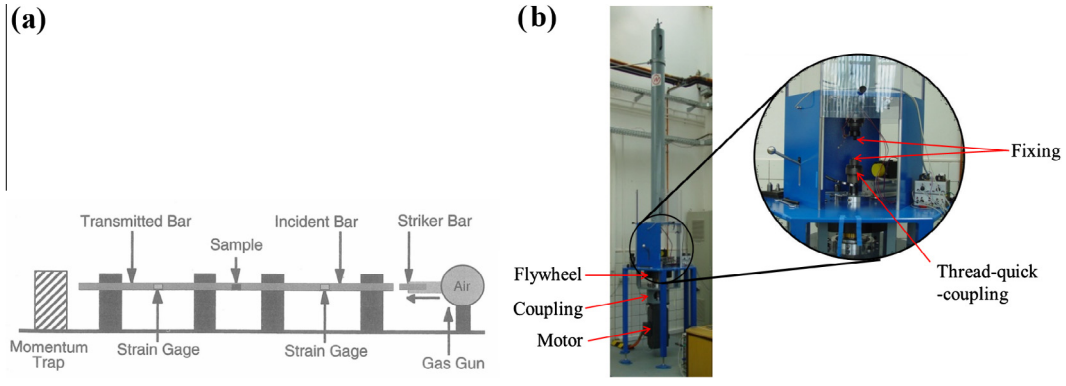

Fig. 2. Test devices: (a) Schematic of a compression Split-Hopkinson-Pressur-Bar (SHPB) Handbook, 2002, (b) Torsion test machine.

of one dimensional elastic wave propagation in slim bars, the stress–strain response of the material can be calculated.

Torsion tests: Experimental investigations under torsion loading are performed using a high rate testing machine, which is available at Chemnitz University of Technology, see Fig. 2(b). The machine is developed for experimental investigations of materials under monotonic and cyclic torsion loading. Furthermore, a wide range of strain rates from 10^{-3} to 10^{-2} s^{-1} can be realized in the machine. For the dynamic tests at strain rates of 10^{-2} s^{-1}, the specimen is fixed at the lower end of a Hopkinson bar. According to the principle of a flywheel machine, a flywheel mass is accelerated. If the required testing velocity is reached, the specimen is impact loaded up to failure using a thread-quick-coupling device. Applying the Hopkinson principle, the torque of the specimen is measured using the Hopkinson bar. At room temperature, the transition from elastic to elastic–plastic flow of the specimen is measured with a strain gage applied directly on the specimen. Higher plastic deformations and the plastic deformation at high temperature torsion tests are calculated from the torsion angle. The specimens were heated using an inductive heating device.

The resulting stress strain curves are shown in Fig. 3. As can be seen e.g. in Fig. 3(a) (from the data with symbols), the elastic behavior is identical for different strain rates. However, the inelastic behavior changes with strain rate, the higher the strain rate, the

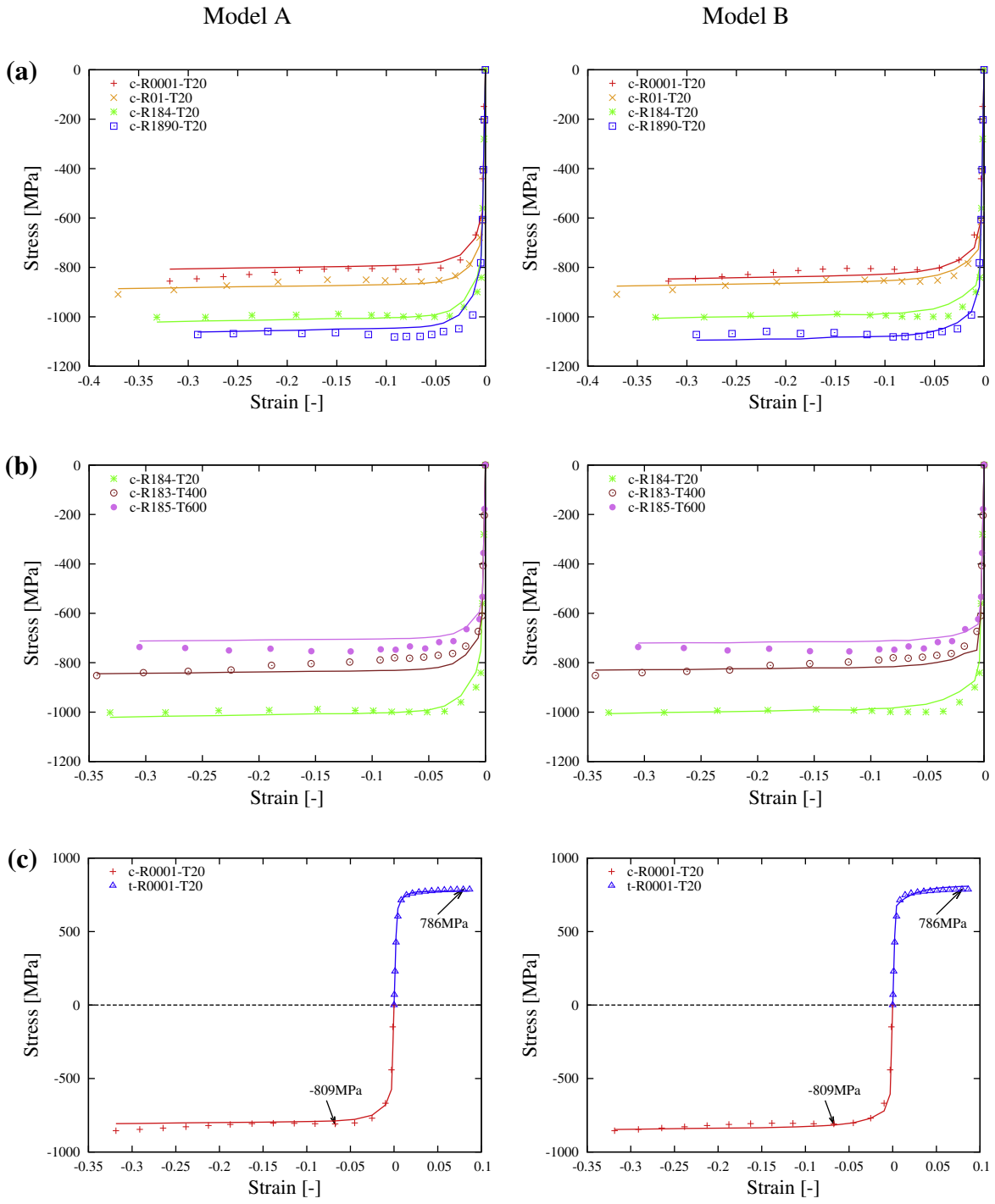

Fig. 3. Steel 100cr6: Stress strain curves (a) under compression with same temperature, different strain rates, (b) different temperatures, almost same strain rate and (c) under tension and compression with same temperature and strain rate. Symbols refer to experiment, solid lines to simulation.

larger the yield stress. Additionally, the stress–strain curves in Fig. 3(b). illustrate the temperature dependence. The results in Fig. 3.c show the asymmetric effect of the inelastic behavior (786 MPa for tension, −809 MPa for compression), where both curves are obtained with same strain rate and same temperature. In addition, the results for the tests s-R101-T20 and s-R101-T600 in Fig. 4(a), reveal a different inelastic behavior for torsion in comparison to tension and compression. Lastly, the results in Fig. 4(b) show shear stress–strain curves with temperature dependence.

For parameter identification based on experimental testing a least-squares functional is considered as an identification criterion in order to minimize the distance of the simulated data to the experimental data. The least-squares problem reads:

$$f(\kappa) = \tfrac{1}{2}\|\mathbf{d}(\kappa) - \overline{\mathbf{d}}\|_2^2 \to \min(\kappa \in \mathcal{K}), \text{ where}$$
$$\mathcal{K} = \prod_{i=1}^{n_p} \mathcal{K}_i, \ \mathcal{K}_i := \{a_i \leqslant \kappa_i \leqslant b_i\} \tag{80}$$

Here, $\mathbf{d}(\kappa)$ are the simulated data, which depends on the parameters. a_i, b_i are lower and upper bounds for the material parameters.

A general framework and technical details for the minimization of the least-squares functional is presented elsewhere, see e.g. Mahnken et al., 1998; Mahnken, 2004 for more details, which shall not be considered here.

The constitutive equations of Section 3 for Model A and Model B of Table 1 and 2 have been used. In both cases we set $S = 3$ for the number of modes, thus referring to three types of experiments in

Table 5
Material parameters for steel 100Cr6

κ_{el}:	E_0 [MPa]	ν[−]	$c_E[\frac{\text{MPa}}{^\circ\text{C}}]$	$\theta_{E_0}[^\circ\text{C}]$	
	2.06E + 05	0.28	0.0	20	
κ_{pl}^{MA}:	Y_{01} [MPa]	Y_{02} [MPa]	Y_{03} [MPa]	H_1 [MPa]	H_2 [MPa]
	593.755	571.513	508.065	1.969E + 06	41.29
	c_1[−]	c_2[−]	c_3[−]	C_1[−]	C_2[−]
	141.9	119.13	119.13	2.32E-02	1.92E-02
	C_3[−]	$\dot{\varepsilon}_{01}$[−]	$\dot{\varepsilon}_{02}$[−]	$\dot{\varepsilon}_{03}$[−]	m_1[−]
	1.92E-02	1.E-05	1.E-05	1.E-05	1.56
	m_2[−]	m_3[−]			
	1.56	1.28			
κ_{pl}^{MB}:	Y_0 [MPa]	H_1 [MPa]	H_2 [MPa]	c[−]	m[−]
	666.39	4.47E + 05	92.4	57.04	1.19
	K_1[−]	K_2[−]	K_3[−]	n_1[−]	$n_{2[-]}$
	34.2	71.2	71.2	2.664	5.63
	n_3[−]				
	5.63				
κ_θ:	$\alpha_M[\frac{1}{^\circ\text{C}}]$				
	0.884e-5				
κ_{tp}:	$K_{tp1M}[\frac{1}{\text{MPa}}]$	$K_{tp2M}[(\frac{1}{\text{MPa}})^2]$	μ_{MA}[−]	$k_\theta[\frac{1}{^\circ\text{C}}]$	
	1.03E-04	−0.13E-06	0.0012	0.013	
κ_{tc}:	$\lambda_\theta[\frac{\text{W}}{\text{mm}\cdot^\circ\text{C}}]$	$c_d[\frac{\text{J}}{\text{kg}\cdot^\circ\text{C}}]$			
	4.6E-02	4.52E + 02			
κ_{co}:	$\theta^m[^\circ\text{C}]$	$\theta^r[^\circ\text{C}]$	$\rho_M[\frac{\text{kg}}{\text{mm}^3}]$	$\rho_A[\frac{\text{kg}}{\text{mm}^3}]$	$A_{c1}[^\circ\text{C}]$
	1420	20	7.61	7.588	614
	$\theta_{MS}[^\circ\text{C}]$				
	211				

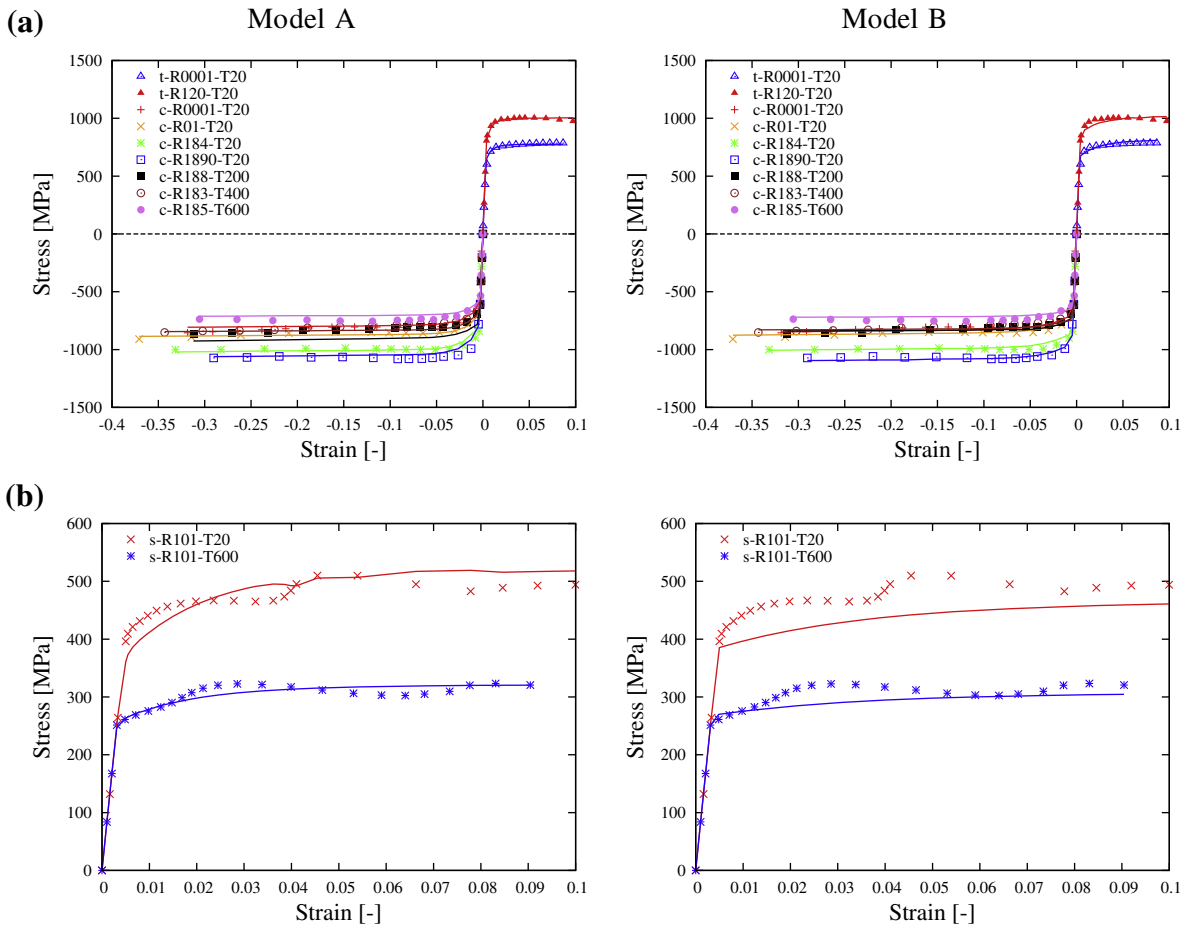

Fig. 4. Steel 100cr6: Stress–strain curves under (a) tension and compression, (b) torsion. Symbols refer to experiment, solid lines to simulation

tension, compression and shear. Analogously to the procedure in Mahnken (2003) the material parameters were obtained in a consecutive manner, firstly for model A the tension–compression data were used to obtain parameters $Y_{01}, H_{11}, H_{21}, c_1, c_{\theta 1}, C_1, \dot{\varepsilon}_{01}, m_1$ for tension as well as $Y_{02}, H_{12}, H_{22}, c_2, c_{\theta 2}, C_2, \dot{\varepsilon}_{02}, m_2$ for compression and in a second phase the shear data were added thus obtaining $Y_{03}, H_{13}, H_{23}, c_3, c_{\theta 3}, C_3, \dot{\varepsilon}_{03}, m_3$ to the final results summarized in Table 5 (κ_{pl}^{MA}). Analogously the parameters for model B are obtained and summarized in Table 5 (κ_{pl}^{MB}).

The comparison of the simulated data to the experimental data is also shown in Fig. 3.a to Fig. 4.b, where the solid lines refer to simulated data. In all diagrams, both for Model A and Model B a good agreement between experiment and simulation is obtained for both models. However, we are aware, that more tests are required to get more data for a convincing parameter-identification.

4.1.2. Dilatometer tests

For determination of material parameters representing the stress–strain response of the under cooled austenite and the TRIP part of the material 100Cr6 (1.3505), so called dilatometer tests are used, which were performed by Stiftung Institut für Werkstofftechnik (IWT), University of Bremen. The thermo-mechanical simulator Gleeble (R) 3500 is used which combined the properties of a hydraulic testing machine with those of a quenching dilatometer. The machine was upgraded by a laser extensometer which allows the measurement of longitudinal and transversal strains. On details for specimen preparation and the loading process we refer to Ahrens (2003). Results on parameter identification for phase transformation are given in Mahnken et al. (2009) and Mahnken et al. (2010). Details on the geometry and preparation of the hollow cylindrical specimens are given in Irretier (2008).

The program for the specimens of temperature and stress is illustrated in Fig. 5.a: The specimens are heated with constant heating speed 6.2 K/s to the austenitizing temperature (850 °C). Then temperature is hold fixed for 10 min for the homogenization of the specimens in the measured length. Then the specimens are cooled with quenching gas (-170 °C), thus resulting into complete martensitic transformation. A schematic illustration of

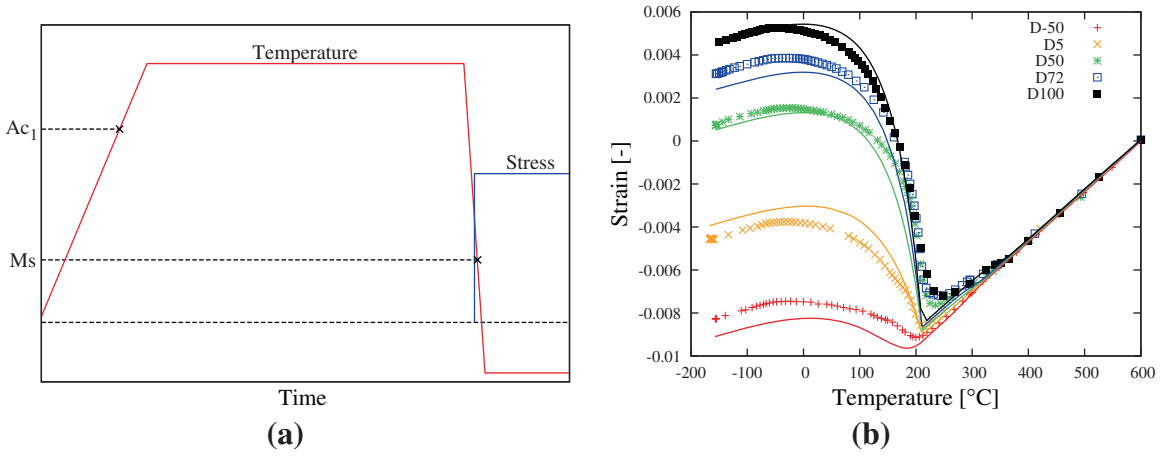

Fig. 5. (a) Phase transformation for 100Cr6: schematic of temperature and stress loading with respect to time; (b) Phase transformation for 100Cr6: longitudinal strain-temperature curves. Comparison of experimental and computed results (symbols refer to experiment, solid lines refer to simulation)

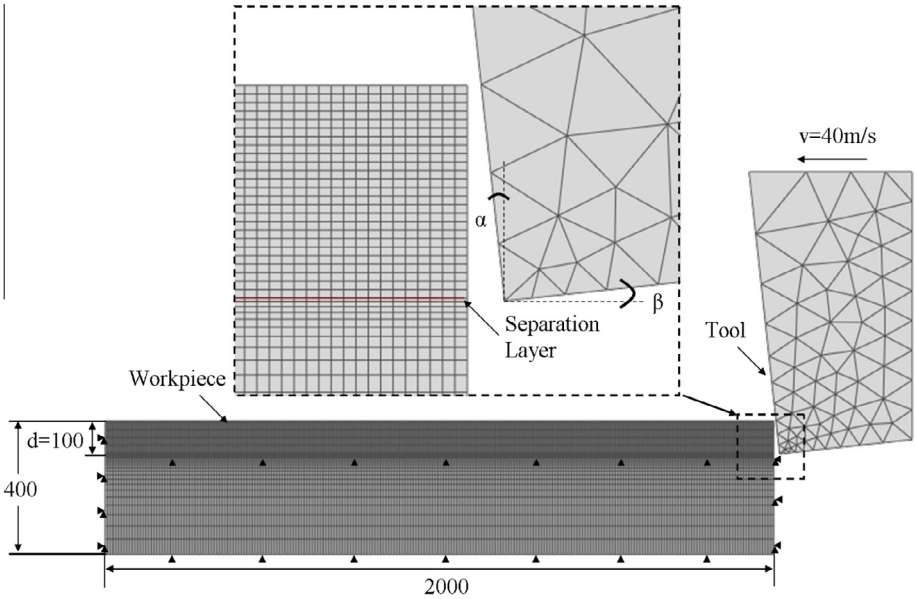

Fig. 6. Cutting simulation: Geometry and finite-element discretization

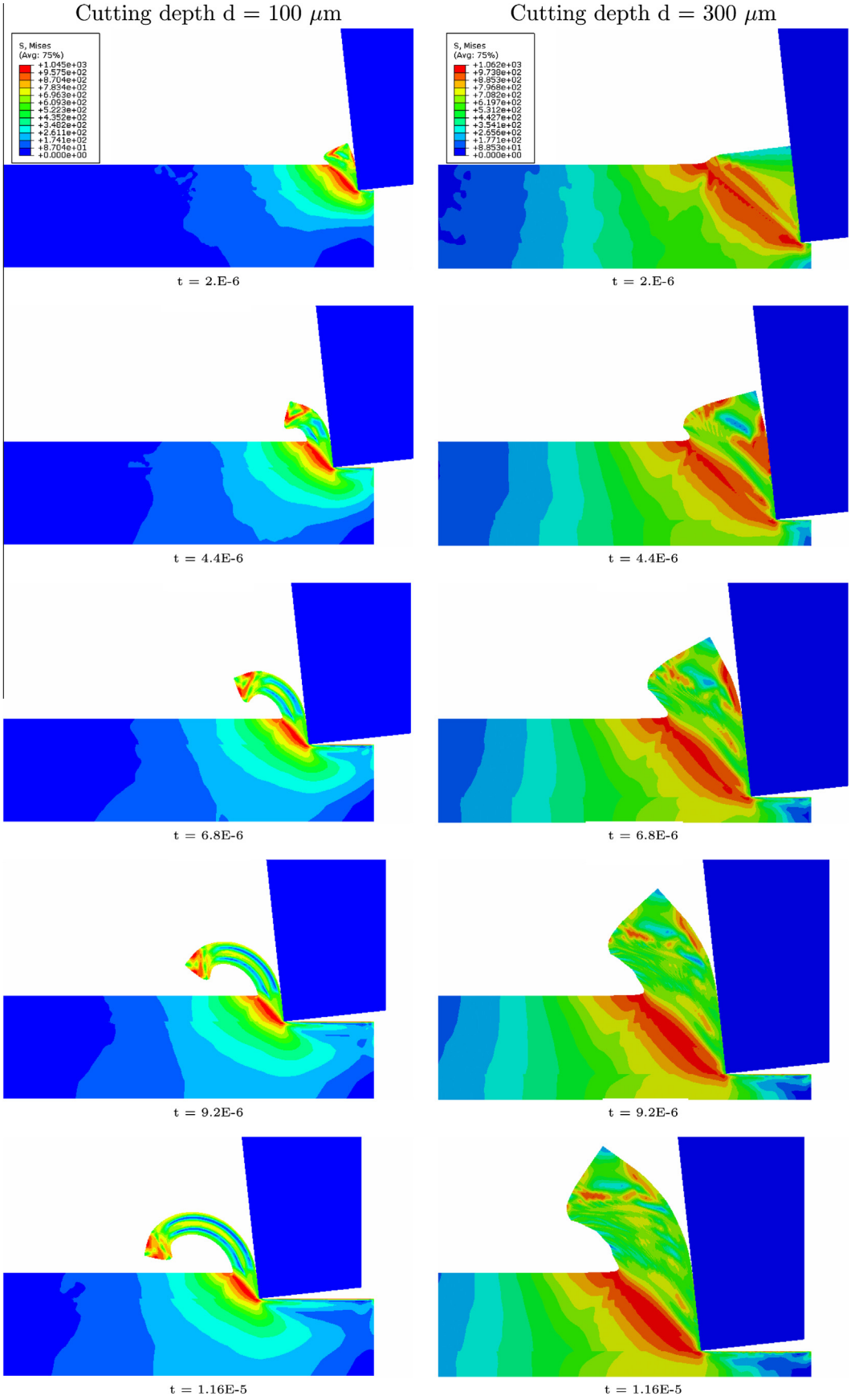

Fig. 7. Cutting simulation: Contours of von-Mises stress for cutting depths 100 μm (left column) and 300 μm (right column)

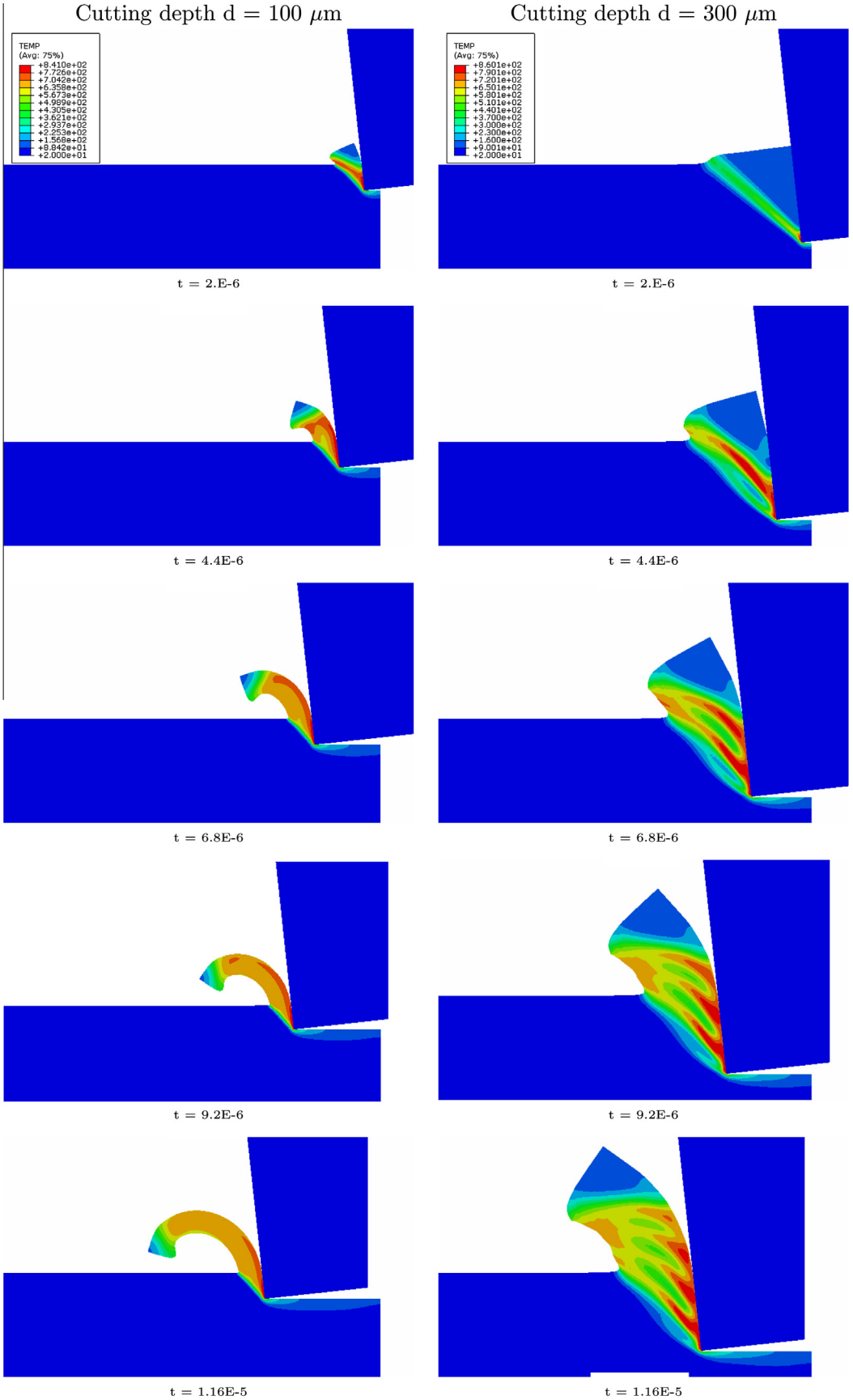

Fig. 8. Cutting simulation: Contours of temperature for cutting depths 100 μm (left column) and 300 μm (right column)

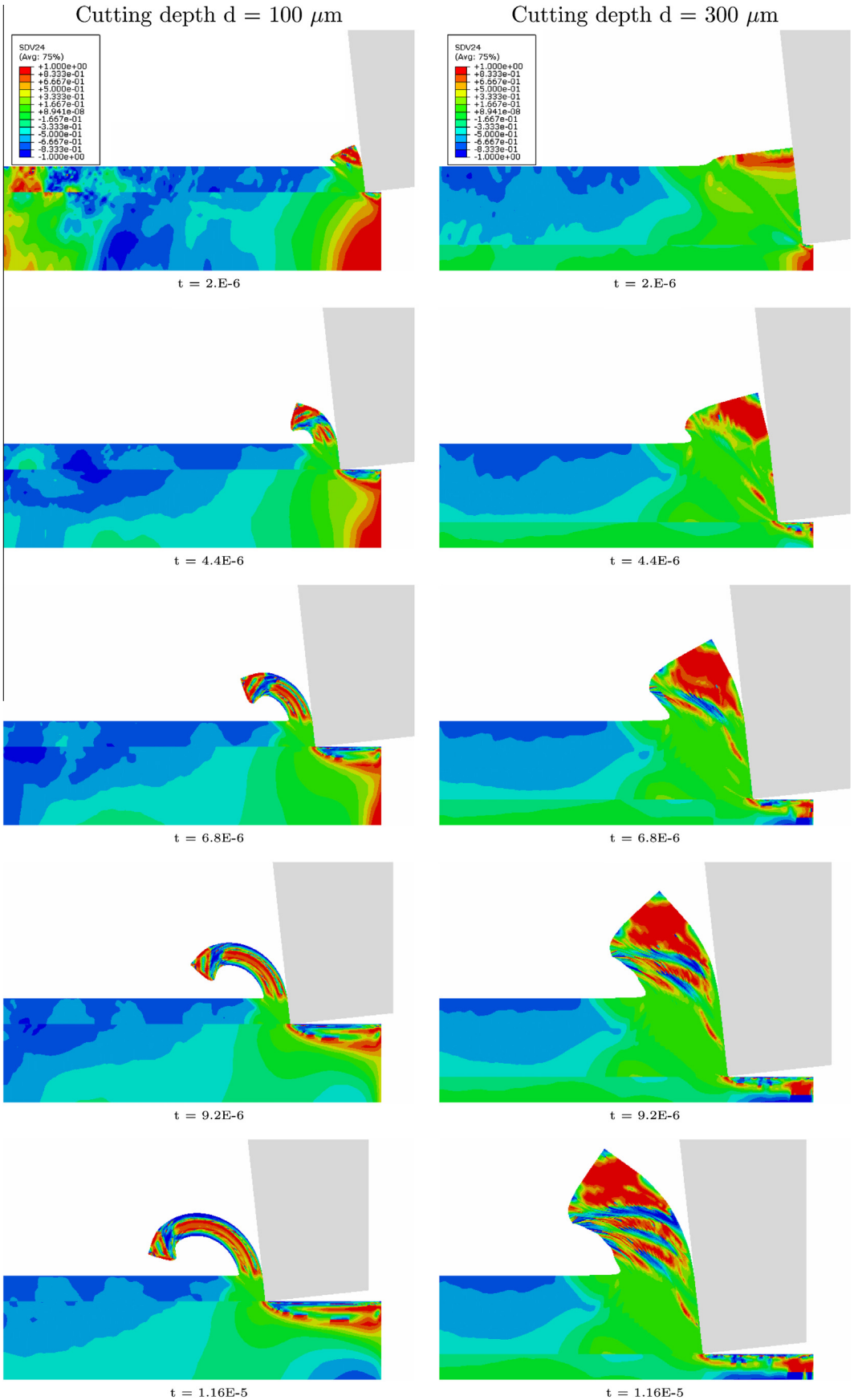

Fig. 9. Cutting simulation: Contours of stress mode factor for cutting depths 100 μm (left column) and 300 μm (right column)

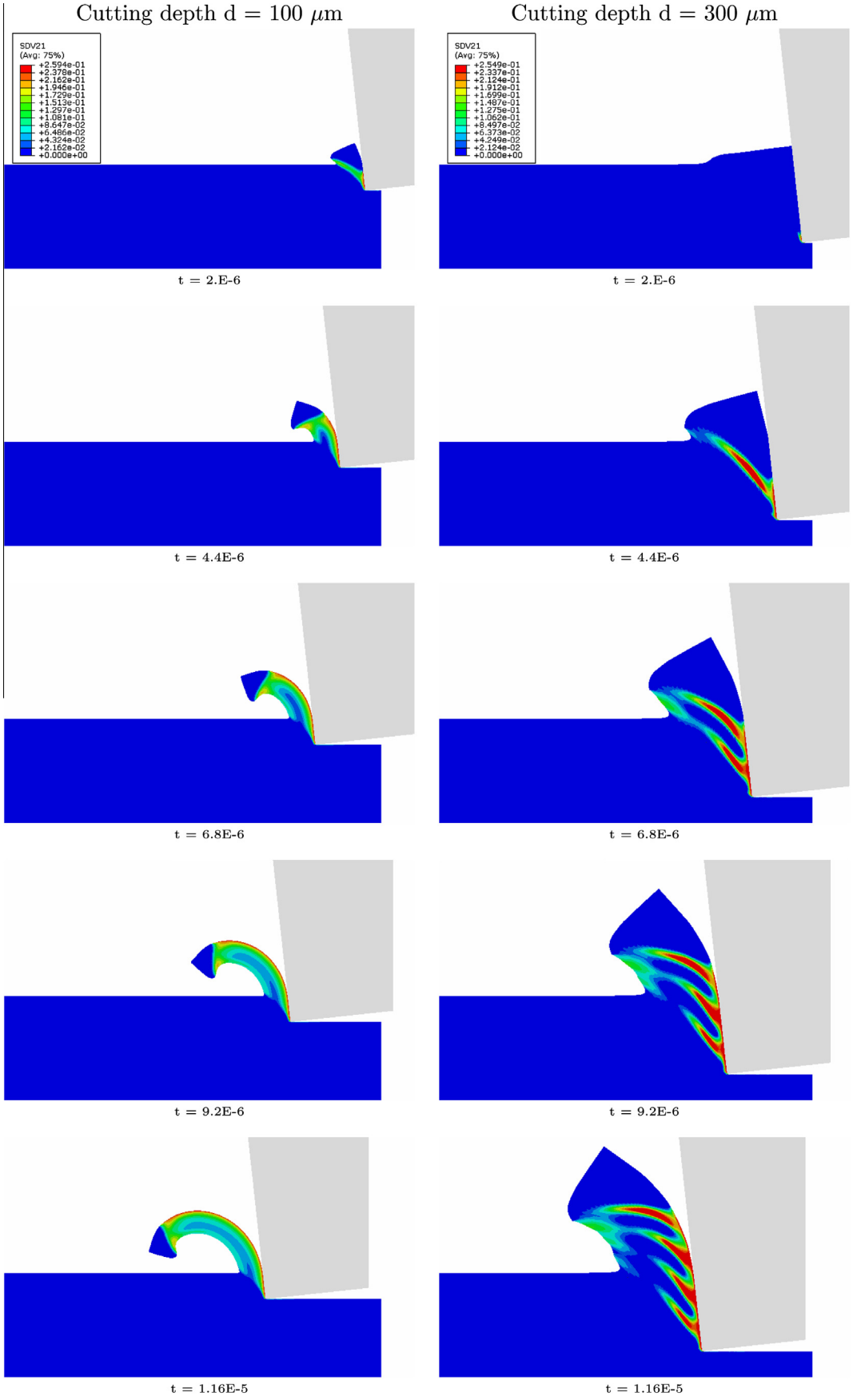

Fig. 10. Cutting simulation: Contours of austenite volume fraction for cutting depths 100 μm (left column) and 300 μm (right column)

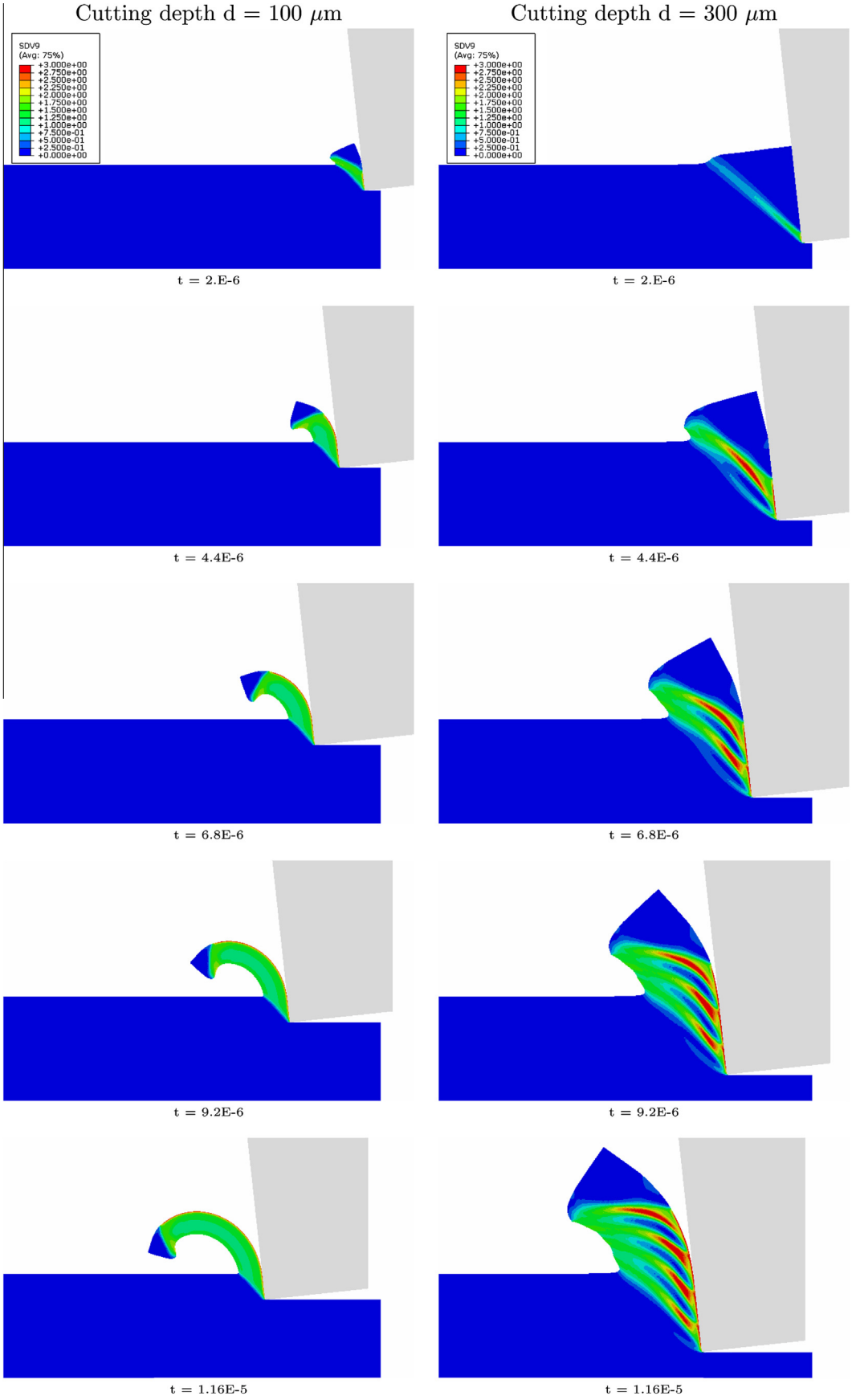

Fig. 11. Cutting simulation: Contours of equivalent plastic strain for cutting depths 100 μm (left column) and 300 μm (right column)

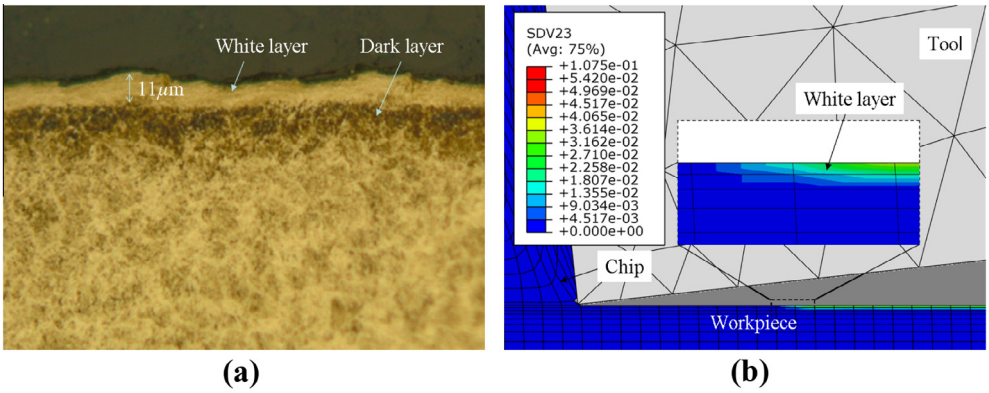

Fig. 12. White layer of 100Cr6: (a) Real illustration (IWF, Berlin), (b) Illustration of new transformed martensite.

temperature and stress loading with respect to time is shown in Fig. 5.a. In order to study the effects of external stresses on the phase transformation behavior, tensile stresses (5 MPa, 50 MPa, 72 MPa and 100 MPa) and compressive stress (-50 MPa) are applied during under cooling. These are applied, when the temperature is approximately 100 °C to 150 °C above the martensitic start temperature. The testing device allows a simultaneous strain measurement in the longitudinal and radial direction. With these data the TRIP strain, the volume strain and the fraction of the transformed phase can be calculated, see Ahrens (2003) and Irretier (2008). Fig. 5 shows longitudinal strain-temperature curves under tension and compression for experimental results. So far experimental results are available with data according to the following nomenclature:

Notation	Stress [MPa]
D-50	−50
D5	5
D50	50
D72	72
D100	100

Analogously to the procedure in Mahnken et al. (2009) the parameters for transformation induced plasticity are obtained and summarized in Table 5. The resulting simulations for the longitudinal strain-temperature curves under tension and compression are also shown in Fig. 5. A satisfying agreement with experimental data is obtained.

4.2. Simulation of a cutting process

In this example a cutting process is investigated in order to test our material model. For all performed calculations the explicit dynamics procedure with full thermo-mechanical coupling is used. The geometry and the finite-element discretization are shown in Fig. 6. The geometry of the tool is described be an negative rake angle $\alpha = -6^\circ$, an clearance angle $\beta = 6^\circ$. The dimensions of workpiece (2D) are length 2000 μm, height 400 μm. The boundary conditions on the workpiece are applied at the bottom, left side, the cutting face as well as the right side under the cutting surface, while the tool move in horizontal direction with constant velocity $v = 40\ ms^{-1}$. The initial conditions assume the room temperature, and a conventional cooling condition is applied over the surfaces of the workpiece. A 4-node plan strain thermally coupled quadrilateral element (CPE4RT) is used for the workpiece and the tool. High mesh density is defined around the cutting surface of the workpiece and the cutting edge of the tool.

Our model was implemented as a user-defined subroutine (VUMAT) linked to Abaqus v6.9 and used to simulate asymmetric plastic material behavior taking account phase tranformation of the workpiece (Abaqus, 2009), and to a separation layer as shown in Fig. 6 we assigned a shear failure criterion for separating the chip from the workpiece. The tool was modeled as purely elastic with high elastic modulus. To the material behavior of the workpiece the constitutive equations in Section 3 with Model A were used. Concerning the similarity of Model A and Model B according to the parameter identification as illustrated in Fig. 3 and 4, a comparison of simulation results with different cutting depths is more meaningful than with different models. Next, the comparison of the von-Mises stress, temperature, stress mode factor, austenite volume fraction and equivalent plastic strain for cutting depths $d = 100\mu m$ and $d = 300\mu m$ at time instant $2.0 \cdot 10^{-6}, 4.4 \cdot 10^{-6}, 6.8 \cdot 10^{-6}, 9.2 \cdot 10^{-6}$ and $1.16 \cdot 10^{-5}$ are presented in Fig. 7–11, respectively.

Obviously, for both simulations continuous chips are mainly formed, and the chip for the smaller cutting depth $d = 100\mu m$ is more blended. In contrast, the chip for cutting depth $d = 300\mu m$ shows the tendency to form segmented chip as the cutting depth rises. Fig. 7 shows that the von-Mises stress concentrate on the shear zone. Due to mechanical dissipation the temperature locates near the tool tip in the deformation zone of the workpiece as shown in Fig. 8. In Fig. 9, the contours of stress mode factor ξ as described in Section 3.4.1 for indicating the stress modes shows the existence of tension, compression and shear zone. In Ramesh et al., 2007 was reported, that due to the effect of pressure and plastic strain on phase transformation temperatures a reduction of the A_{c1} temperature at which austenite formation starts needs to be considered. Therefore, we taken 614°C as the A_{c1} temperature in stead of the nominal austenitization temperature 732°C for 100Cr6. The evolutions of austenitic transformation are shown in Fig. 10. Due to rapid cooling the austenitic phase retransforms to martensite once the temperature reaches the martensite start temperature M_s. The new transformed martensite is illustrated in Fig. 12.b, which dominates white layer formation Ramesh et al., 2007. Fig. 12.a gives a microscopic illustration of the white layer of the material DIN 100Cr6, which was experimentally made by the project partner in the frame of the german research program SPP 1480, Institute for Machine Tools and Factory Management (IWF), Technical University Berlin.

5. Summary and conclusions

In this paper we have developed a multimechanism model for simulation of visco-plastic material behavior accompanied by phase transformations. The model is formulated within a thermo-

dynamic framework for large strains. This general model has been specialized and applied to a cutting process in steel production. To this end the model of Johnson–Cook is extended to take into account visco-plastic asymmetric effects and transformation induced plastictiy. We are aware of its weakness, since it is not based on underlying physics such as dislocation theory. As a consequence, it should not be used outside the domain, where data exist. In the future, the methology developed on a thermodynmics framework in this paper will be extended to different models, such as the Zerilli-Armstrong model Zerilli et al., 1987.

The phase transformations under consideration are: Transformation of the martensitic initial state into austenite, then retransformation to martensite. Thermodynamic consistency of the model developed has been proven. Moreover, this result does not depend on possible modifications within the evolution equations of phase transformations and of TRIP. The finite-element simulation of mechanical behavior and phase transformations in a cutting process demonstrates the capability of the model developed to simulate realistically this process.

Concerning further extensions, the model should consider microscopically based observations. As mentioned in Tjahjanto et al. (2008) and Iwamoto and Tsuta (2004) this would enable to take into account the effect of anisotropy due to crystallographic orientations and in this way would provide a detailed insight into the influence of the microstructure on the overall response.

A more extensive data basis is required in future to verify the model presented in a broader sense and to allow to validate modified approaches of modeling phase transformations and TRIP. Moreover, on the numerical side, an adaptive strategy taking strong mesh distortions during a cutting process into account is an area of future research work.

Acknowledgements

This paper is based on investigations of SPP 1480 which is kindly supported by the Deutsche Forschungsgemeinschaft (DFG). Moreover, it has been partially supported by the Deutsche Forschungsgemeinschaft (DFG) via the Collaborative Research Center SFB 570 "Distortion Engineering" at the University of Bremen.

Furthermore, we gratefully acknowledge the support of the company NORDMETALL, Adorf, Germany, for performing the thermal–mechanical tests, whose specimens were prepared by IWF, and Stiftung Institut für Werkstofftechnik (IWT), University of Bremen, for performing the dilatometer tests in Section 4.1.

References

Abaqus, Dassault Systemes Simulia Corp., 2009, Providence, RI, USA, Theory manual - Version 6.9-1.

Altenbach, H., Altenbach, J., Zolochevsky, A., 1995. Erweiterte Deformationsmodelle und Versagenskriterien der Werkstoffmechanik. Deutscher Verlag für Grundstoffindustrie, Stuttgart.

Ahrens, U., 2003. Beanspruchungsabhängiges Umwandlungsverhalten und Umwandlungsplastizität niedrig legierter Stähle mit unterschiedlich hohen Kohlenstoffgehalten, Dissertation. University of Paderborn, Germany.

Handbook, A.S.M., 2002. Mechanical testing and evaluation. Materials Part Ohio, 8.

Attanasio, A., Umbrello, D., Cappellini, C., Rotella, G., M'Saoubi, R., 2011. Tool wear effects on white and dark layer formation in hard turning of AISI 52100 steel. Wear 286–287 (2012), 98–107.

Behrens, A., Westhoff, B., Kalisch, K., 2005, Application of the finite element method at the chip forming process under high speed cutting conditions, in Tönshoff, H.K., Hollmann, F. (editors), Hochgeschwindigkeitsspanen, p. 112-34, Wiley-vch

Betten, J., Sklepus, S., Zolochevsky, A., 1998. A creep damage model for initially isotropic materials with different properties in tension and compression. Eng. Fract. Mechs. 59 (5), 623–641.

Betten, J., Sklepus, S., Zolochevsky, A., 1999. A microcrack description of creep damage in crystallin solids with different behaviour in tension and compression. Int. J. Damage Mechanics 8, 197–232.

Cailletaud, G., Saï, K., 1995. Study of plastic/viscoplastic models with various inelastic mechanisms. Int. J. Plast. 11, 991–1005.

Cherkaoui, M., 2002. Transformation induced plasticity: Mechanisms and Modeling. Journal of Eng. Mats. Tech. 124, 55–61.

Denis, S.; Simon, A.; Beck, G., 1983, Analysis of the thermomechanical behaviour of steel during martensitic quenching and calculation of internal stresses, Macherauch, E., Hauk, V. (Hrsg.), 211–238.

Dudzinski, D., Molinari, A., 1997. Modelling of cutting for viscoplastic materials. Int. J. Mech. Sci. 39 (4), 369–389.

Ehlers, W., 1995. A single-surface yield function for geomaterials. Archive of Applied Mechanics 65, 246–259.

Fischer, F.D., Sun, Q.-P., Tanaka, K., 1996. Transformation-induced plasticity (TRIP). ASME Appl. Mech. Rev. 49, 317.

Fischer, F.D., Oberaigner, E.R., Tanaka, K., Nishimura, F., 1998. Transformation induced plasticty revised an updated formulation. Int. J. Solids Structures 35 (8), 2209–2227.

Fischer, F.D., Reisner, G., Werner, E., Tanaka, K., Cailletaud, G., Antretter, T., 2000. A new view on transformation-induced plasticity (TRIP). Int. J. of Plasticity 16, 723–748.

Greenwood, G.W.; Johnson, R.H., 1965, The deformation of metals under small stresses during phase transformation, Proc. Roy. Soc., London, Ser. A., A283, 403.

de Groot, S., Mazur, P., 1984. Non-Equilibrium Thermodynamics. Dover Publications, New York.

Hallberg, H., Hakansson, P., Ristimaa, M., 2007. A constitutive model for the formation of martensite in austenitic steels under large strain plasticity. Int. J. of Plasticity 23, 1213–1239.

Halle, T., 2005. Zusammenhänge zwischen Spanvorgängen und dem mechanischen Werkstoffverhalten bei hohen Dehnungsgeschwindigkeiten. Technical University of Chemnitz, Germany, Dissertation.

Haupt, P., 2002. Continuum Mechanics and Theory of Materials. Springer-Verlag, Berlin.

Hortig, Ch., 2010. Local and non-local thermomechanical modeling and finite-element simulation of high-speed cutting. University of Dortmund, Dissertation.

Irretier, A., 2008. Abschlussbericht Projekt C1 Stoffwertebestimmung, Sonderforschungsbereichs 570 Distorsion Engineering. University of Bremen, Germany.

Iwamoto, T., Tsuta, T., Tomita, T., 1998. Investigation on deformation mode dependence of strain-induced martensitic transformation in TRIP steels and modeling of transformation kinetics. Int. J. Mech. Sci. 40 (2–3), 173–182.

Iwamoto, T., Tsuta, T., 2004. Finite element simulation of martensitic transformation in single-crystal TRIP steel based on crystal plasticity with cellular automata approach, Key Eng. Mater. 274–276, 679–684.

Iwamoto, T., 2004. Multiscale computational simulation of deformation behavior of TRIP steel with growth of martensitic particles in unit cell by asymptotic homogenization method. Int. J. of Plasticity 20, 841–869.

Iwamoto, T., Cherkaoui, M., Sawa, T., 2008. A study on impact deformation and transformation behavior of TRIP steel by finite element simulation and experiment. Int. J. Modern Phys. B 22 (31–32), 5985–5990.

Johnson, G.R., Cook, W.H., 1983 A constitutive model and data for metals subjected to large strain rates and high temperatures, Proc. 7th Int. Symp, on Ballistics, The Hague, pp. 541–547.

Koistinen, D.P., Marburger, R.E., 1959. A general equation prescribing the extent of the austenite-martensite transformation in pure iron-carbon alloys and plain carbon steels. Acta Metallica 7, 59–60.

Leblond, J.B., Devaux, J., 1984. A new kinetic model for anisothermal metallurgical transformations in steels including effect of austenite grain size. Acta Metallurgica 32, 137–146.

Leblond, J.B., 1989. Mathematical modelling of transformation plasticity in steels II: Coupling with strain hardening phenomena. Int. J. of Plasticity 5, 537–591.

Levitas, A.V., Idesman, A.V., Olson, G.B., 1998. Continnum modeling of strain-induced martensitic phase transformation at shear-band intersections. Acta Materialia 47 (1), 219–233.

Mahnken, R., 2001. Strength difference in compression and tension and pressure dependence of yielding in elasto-plasticity. Comp. Meths. Appl. Mech. Eng. 190, 5057–5080.

Mahnken, R., 2003. Creep simulation of asymmetric effects by use of stress mode dependent weighting functions. Int. Journal of Solids & Structures 40, 6189–6209.

Mahnken, R., 2005. Creep simulation of asymmetric effects at large strains by stress mode decomposition. Comp. Meths. Appl. Mech. Eng. 94 (2005), 4221–4243.

Mahnken, R., 2005. Void growth in finite deformation elasto-plasticity due to hydrostatic stress states. Comp. Meths. Appl. Mech. Eng. 194, 3689–3709.

Mahnken, R., Johansson, M., Runesson, K., 1998. Parameter estimation for a viscoplastic damage model using a gradient-based optimization algorithm. Eng. Comput. 15 (7), 925–955.

Mahnken, R., 2004, Identification of material parameters for constitutive equations, In: Encyclopedia of Computational Mechanics, Vol. 2, Chapter 19, Eds. E. Stein, R. de Borst, T.J.R. Hughes, John Wiley and Sons Ltd, Chichester.

Mahnken, R., Schneidt, A., 2010. A Thermodynamic Framework and Numerical Aspects for Transformation-Induced Plasticity at Large Strains. Archives of Mechanics 80, 229–253.

Mahnken, R., Schneidt, A., Antretter, T., 2009. Macro modelling and homogenization for transformation induced plasticity of a low-alloy steel. Int. J. Plasticity 25, 183–204.

Mahnken, R., Wolff, M., Schneidt, A., Böhm, M., 2012. Multi-Phase Transformations at Large Strains - Thermodynamic Framework and Simulation. International Journal of Plasticity 39, 1–26.

Mahnken, R.; Wolff, M.; Schneidt, A., Macro modelling for multi-phase transformations at large strains, European Congress on Computational Methods in Applied Sciences and Engineering (ECCOMAS 2012), J. Eberhardsteiner et al. (eds.), Vienna, Austria, September 10–14, 2012.

Marusich, T., Ortiz, M., 1995. Modelling and Simulation of High-Speed Machining. Int. J. Num. Meths. Eng. 38, 3675–3694.

Miller, M.P., McDowell, D.L.: 1996, Modelling large strain multiaxial effects in FCC polycrystals., Int. J. Plast. Vol. 12(7), 875–902.

Nolting, W., 2010. Grundkurs Theoretische Physik 4. Springer-Verlag, Berlin.

Ozel, T., Zeren, E., 2004. Determination of work material flow stress and friction for FEA of machining using orthogonal cutting tests. Journal of Materials Processing Technology 153–154, 1019–1025.

Raniecki, B., Bruhns, O., 1991. Thermodynamic reference model for elastic-plastic solids undergoing phase transformations. Archives of Mechanics 43, 343–376.

Ramesh, A., Melkote, S.N., 2007. Modeling of white layer formaion under thermally dominant conditions in orthogonal machining of hardened AISI 52100 steel. International Journal of Machine Tools & Manufacture 48, 402–414.

Saï, K., Multi-mechanism models: Present state and future trends, International Journal of Plasticity 27 (2011) 250–281.

Sievert, R., Noack, H.-D., Hamann, A., Lwe, P., Singh, K.N., Knecke, G., Clos, R., Schreppel, U., Veit, P., Uhlmann, E., Zettier, R., 2003. Simulation der Spansegmentierung beim Hochgeschwindigkeits- Zerspanen unter Berücksichtigung duktiler Schädigung. Technische Mechanik 23 (2–4), 216–233.

Simo, J.C.; Hughes, T.J.R., 1998, Computational Inelasticity, Interdisciplinary Applied Mathematics, Vol. 7, Mechanics and Materials, Springer–Verlag.

Stouffer, D.C., Dame, L.T., 1996. Inelastic Deformation of Metals. John Wiley & Sons, New York.

Spitzig, W.A., Sober, R.J., Richmond, O., 1975. Pressure dependence of yielding and associated volume expansion in tempered martensite. Acta Metallurgica 23, 885–893.

Tanaka, K., Sato, Y., 1985. A mechanical view of transformation-induced plasticity. Ingenieur-Archiv 55, 147–155.

Tjahjanto, D.D., Turteltaub, S., Suiker, A.S.J., 2008. Crystallographically based model for transformation-induced plasticity in multiphase carbon steels, Continuum Mech. Thermodyn 19, 399–422.

Turteltaub, S., Suiker, A.S.J., 2005. Transformation-induced plasticity in ferrous alloys. J. Mech. Phys. Solids 53, 1747–1788.

Umbrello, D., Saoubi, R.M., Outeiro, J.C., 2007. The influence of JohnsonâCook material constants on finite element simulation of machining of AISI 316L steel. Int J Mach Tools Manuf. 47, 462–470.

Umbrello, D., Filice, L., 2009. Improving surface integrity in orthogonal machining of hardened AISI 52100 steel by modeling white and dark layers formation. Annals of CIRP 58 (1), 73–76.

Voyiadjis, G.Z., Zolochevsky, A., 1998. Modeling of secondary creep behaviour for anisotropic materials with different properties in tension and compression. Int. J. Plast. 14 (10–11), 388–399.

Voyiadjis, G.Z., Zolochevsky, A., 2000. Modeling of secondary creep behaviour for anisotropic materials with different properties in tension and compression. Int. J. Solids Struct. 37, 3281–3303.

Wolff, M., Böhm, M., Boettcher, S., 2007. Phase transformations in steel in the multi-phase case, general modelling and parameter identification, Berichte aus der Technomathematik, FB 3. Universität Bremen.

Wolff, M., Böhm, M., Suhr, B., 2009. Comparison of different approaches to transformation-induced plasticity in steel. Materialwissenschaften und Werkstofftechnik 40 (5–6), 454–459.

Wolff, M., Böhm, M., Mahnken, R., Suhr, B., 2011. Implementation of an algorithm for general material behaviour of steel taking interaction of plasticity and transformation-induced plasticity into account. Int. J. Numer. Meth. Engng 87, 1183–1206.

Zerilli, F.J., Armstrong, R.W., 1987. Dislocation-mechanics-based constitutive relations for material dynamics calculations. Journal of Applied Physics 61 (5), 1816.

Zolochevskii, A.A., 1989, Modification of the theory of plasticity of materials differently resistant to tension and compression for simple loading processes, Soviet Applied Mechanics (transl. Prikladnaya Mekhanika), 24(12), 1212–1217.

Zolochevskii, A.A., 1990, Method of calculating the strength of mine pipes formed from materials that behave differently under tension and compression, Strength of Materials (transl. Problemy Prochnosti), 22(3), 422–428.

Zolochevsky, A.A., 1991. Creep of isotropic and anisotropic materials with different behaviour in tension and compression. In: Zyczkovski, M. (Ed.), Creep in Structures. Springer-Verlag, Berlin, pp. 217–220.